Dynamics of Intraseasonal Sea Level and Thermocline Variability in the Equatorial Atlantic during 2002–03

WEIQING HAN,* PETER J. WEBSTER,+ JIA-LIN LIN,# W. T. LIU,@ RONG FU,& DONGLIANG YUAN,** AND AIXUE HU++

*Department of Atmospheric and Oceanic Sciences, University of Colorado, Boulder, Colorado
+School of Earth and Atmospheric Sciences, Georgia Institute of Technology, Atlanta, Georgia
#Department of Geography, The Ohio State University, Columbus, Ohio
@Jet Propulsion Laboratory, California Institute of Technology, Pasadena, California
&School of Earth and Atmospheric Sciences, Georgia Institute of Technology, Atlanta, Georgia
**Institute of Oceanology, Chinese Academy of Sciences, Qingdao, China
++National Center for Atmospheric Research, ##Boulder, Colorado

(Manuscript received 6 June 2007, in final form 11 October 2007)

ABSTRACT

Satellite and in situ observations in the equatorial Atlantic Ocean during 2002–03 show dominant spectral peaks at 40–60 days and secondary peaks at 10–40 days in sea level and thermocline within the intraseasonal period band (10–80 days). A detailed investigation of the dynamics of the intraseasonal variations is carried out using an ocean general circulation model, namely, the Hybrid Coordinate Ocean Model (HYCOM). Two parallel experiments are performed in the tropical Atlantic Ocean basin for the period 2000–03: one is forced by daily scatterometer winds from the Quick Scatterometer (QuikSCAT) satellite together with other forcing fields, and the other is forced by the low-passed 80-day version of the above fields. To help in understanding the role played by the wind-driven equatorial waves, a linear continuously stratified ocean model is also used.

Within 3°S–3°N of the equatorial region, the strong 40–60-day sea surface height anomaly (SSHA) and thermocline variability result mainly from the first and second baroclinic modes equatorial Kelvin waves that are forced by intraseasonal zonal winds, with the second baroclinic mode playing a more important role. Sharp 40–50-day peaks of zonal and meridional winds appear in both the QuikSCAT and Pilot Research Moored Array in the Tropical Atlantic (PIRATA) data for the period 2002–03, and they are especially strong in 2002. Zonal wind anomaly in the central-western equatorial basin for the period 2000–06 is significantly correlated with SSHA across the equatorial basin, with simultaneous/lag correlation ranging from −0.62 to 0.74 above 95% significance. Away from the equator (3°–5°N), however, sea level and thermocline variations in the 40–60-day band are caused largely by tropical instability waves (TIWs).

On 10–40-day time scales and west of 10°W, the spectral power of sea level and thermocline appears to be dominated by TIWs within 5°S–5°N of the equatorial region. The wind-driven circulation, however, also provides a significant contribution. Interestingly, east of 10°W, SSHA and thermocline variations at 10–40-day periods result almost entirely from wind-driven equatorial waves. During the boreal spring of 2002 when TIWs are weak, Kelvin waves dominate the SSHA across the equatorial basin (2°S–2°N). The observed quasi-biweekly Yanai waves are excited mainly by the quasi-biweekly meridional winds, and they contribute significantly to the SSHA and thermocline variations in 1°–5°N and 1°–5°S regions.

The National Center for Atmospheric Research is sponsored by the National Science Foundation.

Corresponding author address: Weiqing Han, Dept. of Atmospheric and Oceanic Sciences, University of Colorado, UCB 311, Boulder, CO 80309.
E-mail: whan@enso.colorado.edu

DOI: 10.1175/2008JPO3854.1

1. Introduction

Observations in the equatorial Atlantic Ocean show large-amplitude intraseasonal (defined as the 10–80-day period band) variations in zonal and meridional currents and sea level across the equatorial basin (e.g., Dueing et al. 1975; Weisberg et al. 1979; Weisberg and Horigan 1981; Weisberg 1984; Weisberg and Colin 1986; Houghton and Colin 1987; Katz 1987, 1997; Legeckis and Reverdin 1987; Weisberg and Weingartner 1988; Musman 1989, 1992; Luther and Johnson 1990; Contreras 2002; Caltabiano et al. 2005; Giarolla et al. 2005; Grodsky et al. 2005; Kessler 2005 for a review; Brandt et al. 2006; Bunge et al. 2006, 2007; Lyman et al. 2007). Spectral peaks of currents in 10–40-day- and 40–60-day-period bands have been identified by these observations.

On 10–40-day time scales, both wind-driven equatorial waves and tropical instability waves (TIWs) have been observed. Energetic oscillations near a14-day period have been observed in the equatorial Atlantic basin. Garzoli (1987) showed a significant coherence at 14–16-day periods between the observed zonal wind stress and the ocean surface dynamic height near 28°W and found that the maximum amplitude of the 14-day signal occurred at 3°N. Houghton and Colin (1987) found near 15-day oscillations in observed meridional currents and sea surface temperature (SST) in the Gulf of Guinea during 1984. They suggested that these oscillations are the second baroclinic-mode Yanai waves forced by local meridional winds and contribute significantly to the heat divergence and SST variability. Bunge et al. (2006, 2007) detected near 14-day meridional currents during spring 2002 and speculated that they might be wind-driven first baroclinic-mode Yanai waves. The 14-day oscillations have also been observed at depth on the continental slope off the Angola coast (Vangriesheim et al. 2005). Katz (1987) analyzed inverted echo sounder records and showed dominant Kelvin-wave signals at 10–40-day periods along the equator from 34° to 1°W, suggesting that they are the first baroclinic-mode Kelvin waves driven by zonal wind stress in the midbasin.

Also on 10–40-day time scales, TIWs are suggested to attain their maximum power (e.g., Lyman et al. 2007). The TIWs are often generated during boreal summer and may exist throughout May–January (e.g., Jochum et al. 2004). They have wavelengths of 600–1200 km (e.g., Legeckis 1977; Miller et al. 1985; Legeckis and Reverdin 1987; Halpern et al. 1988; Perigaud 1990; Steger and Carton 1991; McPhaden 1996) and a westward phase speed of 20–50 cm s^{-1} (e.g., Weisberg and Colin 1986; Malardé et al. 1987; Weisberg and Weingartner 1988; Musman 1989, 1992; Katz 1997; Kennan and Flament 2000), and they are strongest in the central basin, away from the eastern or western boundary (Richardson and Philander 1987). Data analysis and theoretical and modeling studies suggest that the TIWs result mainly from barotropic instabilities of the mean zonal currents (Philander 1976, 1978; Weisberg and Weingartner 1988; McCreary and Yu 1992; Qiao and Weisberg 1995; Jochum et al. 2004; Johnson and Proehl 2004). Baroclinic (Cox 1980; Hansen and Paul 1984; Luther and Johnson 1990; Baturin and Niiler 1997; Masina et al. 1999; Grodsky et al. 2005), frontal (Yu et al. 1995), and Kelvin–Helmholtz instabilities (Proehl 1996) also contribute.

Few observational studies have shown distinct spectral peaks at 40–60-day periods in near-surface zonal currents. Katz (1997) used 200 days of data from five inverted echo sounders deployed along the equatorial Atlantic during 1983–84 and showed a sharp spectral peak of energy density near 54-day periods. The near 54-day variability has an eastward phase propagation and is thought to be a baroclinic Kelvin wave of mode 1 driven by the zonal winds in the western equatorial basin. Brandt et al. (2006) analyzed data from 11 cross-equatorial ship sections taken at 23°–29°W during 1999–2005 and data from moored Acoustic Doppler Current Profilers (ADCP) at 23°W on the equator during February 2004–May 2005 and found significant spectral peaks at 35–60 days in zonal surface currents. The 35–60-day peaks did not possess a meridional current component (their Fig. 4a), indicating that TIWs may not be the sole cause of the variability.

Although extensive modeling and theoretical studies on TIWs exist, the role intraseasonal winds play in generating oceanic variability in the equatorial Atlantic remains unclear. Although wind-driven equatorial Kelvin and Yanai waves have been identified in observations (Garzoli 1987; Houghton and Colin 1987; Katz 1987, 1997; Bunge et al. 2006, 2007), modeling studies that investigate the detailed dynamics have not yet been done. Hence, a thorough and comprehensive investigation on the relative roles of wind-driven equatorial waves and TIWs in causing intraseasonal variability is needed. There is ample evidence of high-amplitude intraseasonal wind and rainfall variability in the equatorial Atlantic Ocean. Grodsky and Carton (2001), Janicot and Sultan (2001), and Thorncroft et al. (2003) all indicate that the West African monsoon can significantly affect the equatorial Atlantic Ocean. There is some evidence that Amazon convection can influence winds in the western Atlantic basin (Wang and Fu 2007). Furthermore, the Madden–Julian oscillation (MJO; Madden and Julian 1971, 1972) from the Indo-

Pacific Ocean may propagate into the Atlantic to affect the winds there (Foltz and McPhaden 2004). In summary, it can be expected that intraseasonal wind variability may have a strong influence on oceanic variability.

The overall goal of this paper is to provide a detailed understanding of the role played by intraseasonal winds in causing intraseasonal variability in the equatorial Atlantic Ocean, focusing in particular on the response of sea level and thermocline depth. In addition, the relative importance of wind-forced waves versus TIWs is also addressed. A two-pronged approach toward the solution of this problem is adopted using analysis of data and a series of model experiments. First, available satellite data together with in situ observations are analyzed to document the intraseasonal variability. Second, an ocean general circulation model, the Hybrid Coordinate Ocean Model (HYCOM), is used as a primary tool to investigate the mechanisms. A linear model (LM) is also used to help understand the role played by the wind-driven equatorial waves.

2. Data and models

a. Data

Data from the Pilot Research Moored Array in the Tropical Atlantic (PIRATA; Servain et al. 1998) and satellite remotely sensed observations for the period of interest, 2001–03, are used to document intraseasonal variability. The PIRATA data analyzed in this paper are depths of 20° isotherms (D20) and surface winds at several locations along the equator; ADCP currents at 23°W, 0°N, which were measured at 0-, 10-, 20-, 30-, 50-, 75-, 100-, 125-, 150-, 200-, 250-, 300-, 400-, 500-, 600-, 700-, 800-, 900-, 1000-, and 1100-m depths; and SST. The satellite data include sea surface height anomalies (SSHA), which are from a merged product of Ocean Topography Experiment (TOPEX)/Poseidon, *Jason-1*, and the European Research Satellite (*ERS-1*) altimeter produced by the French Archiving, Validation, and Interpretation of Satellite Oceanographic data (AVISO) project using the mapping method of Ducet et al. (2000). The SSHA data are interpolated onto a global grid of 1/3° resolution, archived weekly, and computed relative to a 7-yr mean from January 1993 to December 1999. In addition, daily scatterometer winds from the Quick Scatterometer (QuikSCAT) satellite and 3-day-mean SST from the Tropical Rainfall Measuring Mission (TRMM) Microwave Imager (TMI; Wentz et al. 2000) for the period of interest are also examined. Although we focus on 2001–03, winds and SSHA for the entire period of July 1999–January 2007 will also be analyzed.

b. The ocean models

1) HYCOM

The HYCOM is documented in detail in Bleck (2002) and Halliwell (1998, 2004). For the current study, it is configured to the tropical Atlantic Ocean 30°S–40°N, with a horizontal resolution of 0.5° × 0.5° and a realistic bottom topography with 5° × 5° smoothing. This resolution can reasonably resolve the scale of the TIWs (Cox 1980), which have typical wavelengths of 600–1200 km. Vertically, 22 sigma layers are chosen with a fine resolution in the upper ocean to better resolve the vertical structures of upper ocean currents, temperature, mixed layer, and thermocline. A reference pressure level of sigma 0 is adopted, because we focus on upper ocean processes. The nonlocal *K*-profile parameterization (KPP) is used for the boundary layer mixing scheme (Large et al. 1994, 1997). The diapycnal mixing coefficient is set to $(1 \times 10^{-7}\ \mathrm{m^2\ s^{-2}})N^{-1}$, where N is the buoyancy frequency. Isopycnal diffusivity and viscosity values are formulated as $u_d \Delta x$, where Δx is the local horizontal mesh size and u_d is 0.03 m s^{-1} for momentum and 0.015 m s^{-1} for temperature and salinity. In regions of large shear, isopycnal viscosity is set proportional to the product of mesh-size squared and total deformation (Bleck 2002), and the proportionality factor used here is 0.1. Solar shortwave radiation penetration is included with Jerlov water type IA (Jerlov 1976).

Along the continental boundaries, no-slip boundary conditions are applied. Near the southern and northern boundaries, sponge layers of 5° (30°–25°S and 35°–40°N) are applied to relax the model temperature and salinity to the Levitus and Boyer (1994) and Levitus et al. (1994) climatologies. Similar versions of HYCOM have been used in the tropical Indian Ocean for studying intraseasonal-to-interannual variability (e.g., Han et al. 2004; Han 2005; Yuan and Han 2006).

Daily QuikSCAT winds (Tang and Liu 1996), net shortwave and longwave radiative fluxes from the International Satellite Cloud Climatology Project flux data (ISCCP-FD; Zhang et al. 2004), and National Centers for Environmental Prediction–National Center for Atmospheric Research (NCEP–NCAR) reanalysis (Kalnay et al. 1996) air temperature and specific humidity are used as surface forcing fields for HYCOM. Precipitation is from the Climate Prediction Center (CPC) Merged Analysis of Precipitation (CMAP) pentad data (Xie and Arkin 1996), which is interpolated to daily resolution before forcing the model. Daily QuikSCAT wind stress is calculated from wind speeds using a drag coefficient of 0.0015. These choices are made based on the best available datasets for the period of interest (see Han et al. 2007).

TABLE 1. Parameters for the LM: c_n is the characteristic speed of baroclinic mode n (=1, 2, 3, 4); D_n is the wind-coupling coefficient for mode n, and the larger the D_n, the stronger is the mode excited by winds; L_k is Kelvin wavelength at the 45-day period (here we use 1° = 111 km); L_r is the first meridional mode Rossby wavelength at 50-day (values outside the parentheses) and 45-day (values within the parentheses) periods; L_{mrg} is the mixed Rossby-gravity wavelength at T = 15 days (outside parentheses) and 28 days (within the parentheses).

Parameter	Mode 1	Mode 2	Mode 3	Mode 4
c_n (cm s^{-1})	227	132	86	62
D_n (m^{-1})	3.5×10^{-3}	9.2×10^{-3}	4.1×10^{-3}	2.4×10^{-3}
L_k (°) T = 45 days	80	46	30	22
L_r (°) T = 50(45) days	26 (22)	12 (NO)	NO	NO
L_{mrg} (°) T = 15(28) days	22 (7.4)	55 (8.3)	62 (10.0)	18 (12.2)

Two versions of the forcing fields are utilized: daily mean, which includes intraseasonal variations, and the low-passed version of the daily field using a Lanczos digital filter (Duchon 1979) with a half-power period at 80 days, which excludes intraseasonal variations. The model is spun up from a state of rest for 20 yr using Comprehensive Ocean–Atmosphere Data Set (COADS) monthly mean climatological fields. Based on the results of yr 20, HYCOM is integrated forward in time using the daily and low-passed 80-day forcing fields of 2000–03 (see section 2c), a period when all of the above forcing fields and PIRATA data (current, D20, and SST) are available. Considering that the first 2 yr of results may contain transient effects induced by switching on of the forcing from monthly climatology to daily fields, we use the results of 2001–03 to obtain the band-pass-filtered fields (see section 3) and focus on analyzing the solutions for 2002–03.

2) THE LM

The linear continuously stratified ocean model is described in detail in McCreary (1980, 1985), and it has been applied to several Indian Ocean studies (e.g., McCreary et al. 1996; Han et al. 2004; Han 2005). Here, it is set up for the tropical Atlantic Ocean. The equations of motion are linearized about a state of rest with a realistic background stratification calculated from the Levitus temperature and salinity averaged over 10°S–10°N (Levitus and Boyer 1994; Levitus et al. 1994). The ocean bottom is assumed to be flat. With these restrictions, solutions can be represented as expansions in the vertical normal modes of the system, with the total solution being the sum of all modes. In this paper, unless specified otherwise, the first 25 baroclinic modes are used and solutions are well converged (not shown). Table 1 lists the characteristic speeds c_n for the first four baroclinic modes estimated from buoyancy frequency N_b, which is calculated from the Levitus data, together with other useful values. The wind-coupling coefficient for mode n (=1, 2, 3, . . .), $D_n = 1/\int_H^0 \psi_n^2(z)\, dz$, indicates the efficiency of wind projection onto each mode. Here, H = 4000 m is the ocean depth and $\psi_n(z)$ is the eigenfunction for the nth baroclinic mode, which is estimated from N_b (for a detailed derivation, see McCreary 1980, 1985). Apparently, winds most effectively project onto the second baroclinic mode. The Laplacian mixing on momentum is included with a coefficient of 5×10^7 cm^2 s^{-1}. The vertical mixing coefficient is $\nu = A/N_b^2$, where $A = 1.3 \times 10^{-4}$ cm^2 s^{-3}.

The model basin, grid points, and continental boundary conditions are the same as those of the HYCOM, except that the LM does not have bottom topography. Closed boundaries are used at the northern and southern boundaries, and a damper on zonal currents is applied within 5° of the boundaries to damp the currents toward zero, thereby reducing the spurious coastal Kelvin waves caused by the artificial boundaries. This is basically consistent with the sponge layer of HYCOM for the same regions. As with HYCOM, the LM is first spun up for 20 yr using the monthly climatology of

TABLE 2. A suite of HYCOM and LM experiments performed for the period 2000–03. (See the text for a more detailed description.)

Experiment	Forcing	Description
HYCOM MR	Daily	Complete
HYCOM EXP	Low-passed 80 day	Remove intraseasonal forcing
LM MR	Daily wind stress	Total wind stress
LM EXP1	Daily zonal wind stress	Zonal wind stress only
LM EXP2	Daily wind stress with a 12° zonal filter within 8°S, 8°N	Remove the winds caused by TIWs

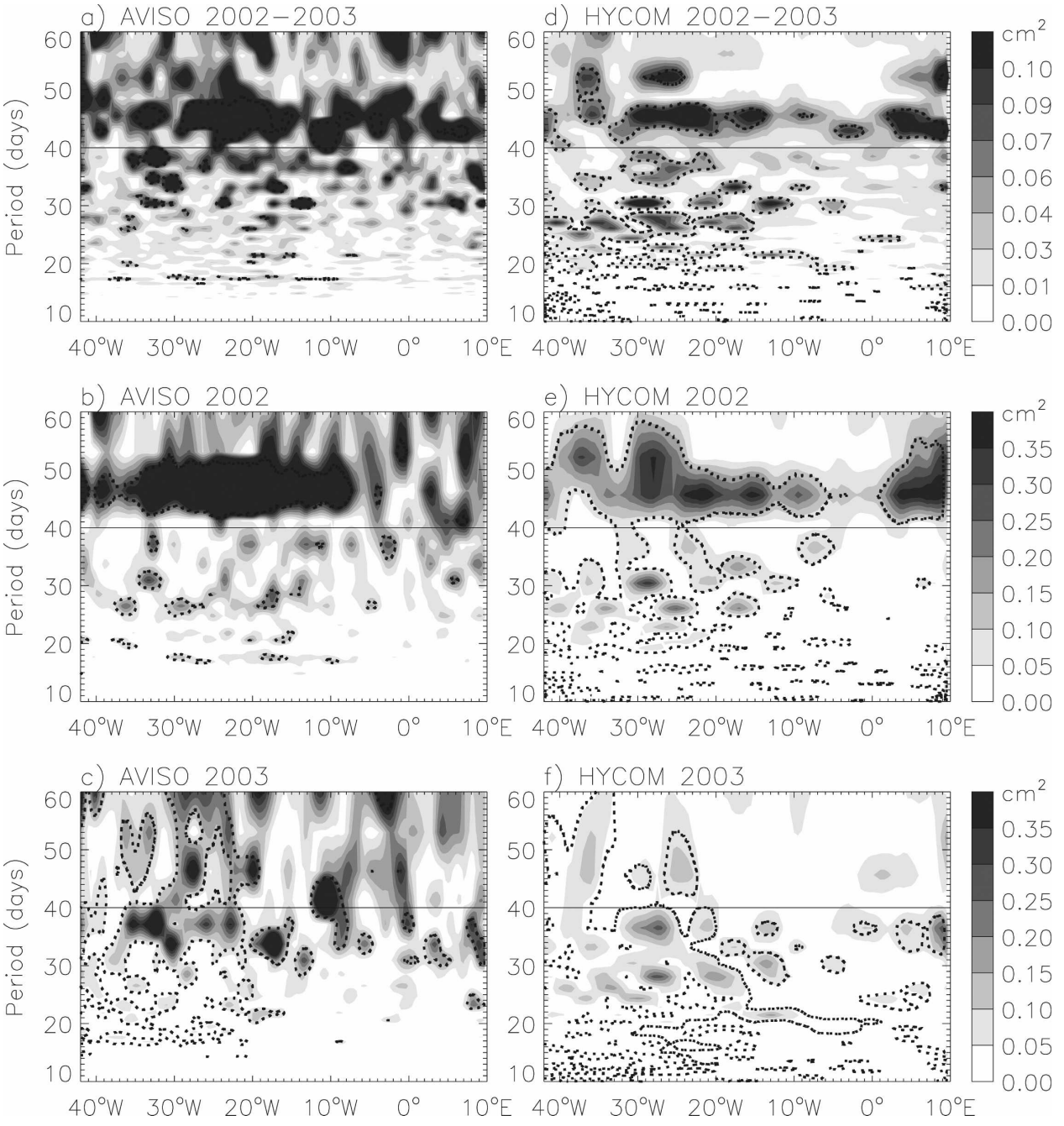

FIG. 1. (a) Variance spectra of SSHA along the equator (averaged over 2°S–2°N) based on AVISO weekly satellite observations for the period of 2002–03; (b) same as in (a), but for 2002; (c) same as in (a), but for 2003; (d)–(f) same as in (a)–(c), respectively, but for the SSHA spectra calculated from the daily HYCOM MR solution. Dashed lines show a 95% significance level. Unit: cm^2.

COADS wind-stress forcing. Restarting from yr 20, the model is integrated forward for the period 2000–03 forced by the daily QuikSCAT wind stress.

c. *Experiments*

Two HYCOM experiments are performed. The experiment HYCOM main run (MR) is forced by the unfiltered daily forcing fields. Intraseasonal variability in the MR results from both intraseasonal atmospheric forcing and TIWs. To assess the role played by TIWs, HYCOM is also forced by the low-passed 80-day fields, which purposely exclude intraseasonal atmospheric forcing and thus wind-forced oceanic intraseasonal variability. [This experiment is referred to as the

HYCOM experiment run (EXP).] To understand the role of wind-driven equatorial waves, the LM, which excludes TIWs, is forced by the unfiltered daily wind stress fields and is referred to as LM MR. To estimate the effects of zonal versus meridional wind stress on equatorial waves, in LM EXP1, the LM is forced by zonal wind stress only. Note that winds over the equatorial Atlantic can also be affected by the feedback from the TIWs (Xie et al. 1998; Liu et al. 2000; Chelton et al. 2001; Hashizume et al. 2001; Caltabiano et al. 2005). To exclude this effect, in LM EXP2, the LM is forced by winds with a spatial filter of a 12° running average in the zonal direction within 8°S–8°N, which works well for removing the TIW signals (Hashizume et al. 2001). These experiments are summarized in Table 2.

3. Results

We first analyze available observations to document intraseasonal variability in the equatorial Atlantic Ocean and compare the HYCOM MR solution with the observations to verify the model performance (section 3a). Next, we examine the hierarchy of HYCOM and LM solutions to gain an understanding of the dynamics of the 40–60-day and 10–40-day variabilities of sea level and thermocline (sections 3b,c). In both sections, we address the roles of wind-forced waves and TIWs in generating the observed variability. Finally, in section 3d we estimate the effects of winds associated with the TIWs.

a. Observed and simulated intraseasonal variability

Figures 1a–c show variance spectra of AVISO weekly SSHA along the equator for 2002–03, 2002, and 2003, respectively. Interestingly, sea level variability shows strong spectral peaks at 40–60 days across most of the equatorial basin, and it dominates in magnitude the 10–40-day variability that contains the TIWs (Fig. 1a). The dominance of 40–60-day SSHA is most apparent in 2002, when the 40–60-day SSHA amplitude is particularly strong and spatially coherent while the 10–40-day variability is especially weak (Fig. 1b). In 2003, SSHA has significant power at both 10–40-day and 40–60-day periods, and the strength and dominant periods of SSHA vary with longitudinal locations (Fig. 1c). The dominance of 40–60-day SSHA in 2002 and the significant power of SSHA at both periods in 2003 are reasonably simulated in the HYCOM MR solution (Figs. 1d–f). Overall, though, the model spectral peaks are weaker than those of observations.

Consistent with the sea level observations, D20 obtained from PIRATA data during 2002–03 shows a sharp 40–50-day spectral peak at both 35° and 23°W on the equator (Figs. 2a,b), with significance exceeding

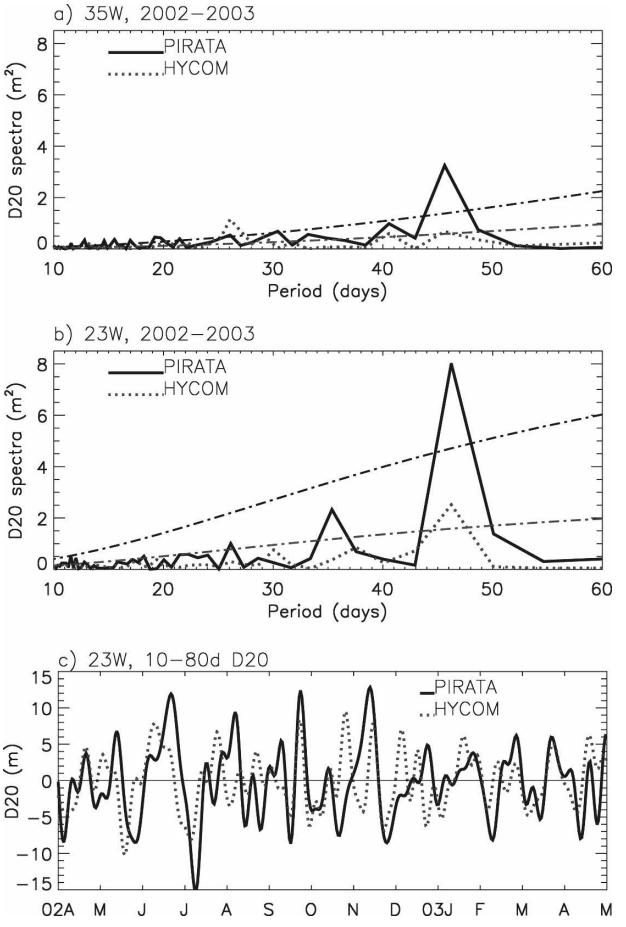

FIG. 2. (a) Variance spectra of 20°C isotherm depth (D20) at 35°W, 0°N from PIRATA data (solid) and HYCOM MR (dashed), based on the period of 2002–03; the corresponding dashed–dotted lines represent 95% significance levels. Note that the seasonal cycle is removed before the spectral analysis is performed. (b) Same as in (a), but for 23°W, 0°N, based on the overlapping model–data period of 1 Jan 2002–24 Aug 2003. (c) The 10–80-day bandpass-filtered D20 at 23°W, 0°N from PIRATA data (solid) and from HYCOM MR (dashed). The 20 months' data (January 2002–August 2003) are used for the filter, but only the period of April 2002–April 2003 is shown to exclude the end point effects of the filter.

95% at both locations. A time series of 10–80-day bandpass-filtered D20 shows that intraseasonal fluctuations of the thermocline vary between −15 and 13 m at 23°W during the 20-month date period. This variation is large compared to the shallow, mean thermocline depth of 78 m obtained from PIRATA data at the same location for the same period of time. HYCOM is able to reproduce the dominant 40–60-day peaks (Figs. 2a,b, dotted lines), but their power is much weaker than the observations. The weak amplitudes of HYCOM intraseasonal SSHA and D20 (Figs. 1, 2) may result from the deeper mean thermocline, which would be less sensitive to the surface forcing. The mean D20 from HYCOM MR is 123

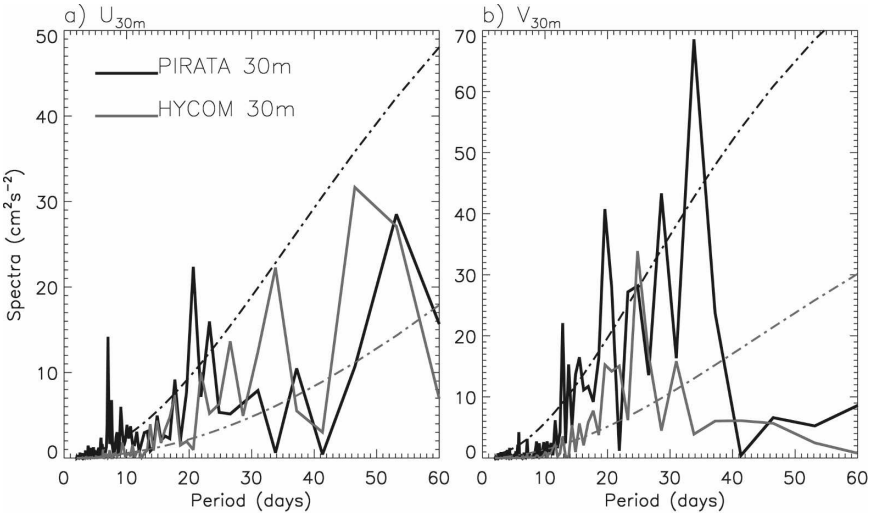

FIG. 3. (a) Variance spectra of zonal current at a 30-m depth based on the daily records during 14 Dec 2001–20 Dec 2002 at 23°W, 0°N from the PIRATA data (black) and HYCOM MR solution (gray). Seasonal cycle is removed before the spectral analysis is performed. The dashed curves show a 95% significance level. The 40–60-day peak did not exceed 95% significance due to the short data record, but it did exceed the 85% significance level (not shown). (b) Same as in (a), but for meridional current. Units: $cm^2\ s^{-2}$.

m at 23°W during the 20-month PIRATA data period, 45 m deeper than that of the PIRATA D20.

The 40–60-day peak is also present in the PIRATA near-surface zonal current at 23°W, 0°N, and no corresponding peak exists in the meridional current (Figs. 3a,b). This may suggest the equatorial symmetric property of the 40–60-day variability, which will be discussed in section 3b. Basically, HYCOM produced the spectral peaks of zonal currents at both the 10–40-day- and 40–60-day-period bands, and peaks of meridional currents at a 10–40-day-period range, although significant model data differences exist, especially at the 10–40-day periods when TIWs are strong (Fig. 3). To quantify how well the TIWs are simulated, we calculate the HYCOM MR perturbation kinetic energy (PKE; see Weisberg and Weingartner 1988 for definition) during 2002–03 at the same location and depths as those of Weisberg and Weingartner (1988). The TIWs reach their maximum energy in summer with an energy peak of 1300 erg cm^{-3} at 10 m and 635 erg cm^{-3} at 75 m in HYCOM MR (not shown), comparing to 1600 erg cm^{-3} at 10 m and 600 erg cm^{-3} at 75 m in Weisberg and Weingartner (1988, their Fig. 6). The peak energy in HYCOM is weaker than the observations at the surface and somewhat stronger at depth, indicating that more energy is mixed downward in HYCOM. The model PKE has a weaker, secondary peak during fall, a feature that was also observed by Weisberg and Weingartner (1988; see also Jochum et al. 2004).

To quantify further the variations of sea level along the equator on intraseasonal time scales, Fig. 4 shows the bandpass-filtered SSHA and D20 averaged over 2°S–2°N from AVISO observations and model solutions in 2002. Because AVISO data have weekly resolution, the periods for the Lanczos bandpass filter are chosen to be 14–80 days. The observed SSHA appears to be dominated by near 45-day oscillations for most of the year (Fig. 4a). An exception is during June–August, when the SSHA patterns are complicated by the westward-propagating, higher-frequency variability. The dominance of the 40–50-day oscillations and the occurrence of strong higher-frequency variability in summer are reasonably simulated by HYCOM MR (Fig. 4b).

Note that HYCOM produces weaker SSHA and D20 and somewhat weaker TIW PKE near the surface than the observations. The quantitative differences between data and model at a specific location may result partly from the influence of TIWs, the deeper D20 in HYCOM, and errors in the model and forcing fields. Nevertheless, HYCOM is able to reasonably simulate the observed intraseasonal peaks of sea level, thermocline depth, and the TIWs, and it is thus a useful tool for the identification of major processes that cause intraseasonal variability.

b. Dynamics of the 40–60-day variability

1) 2002–03

It is interesting to note that the strong 40–50-day SSHA shown in Fig. 4a is reproduced by the LM solu-

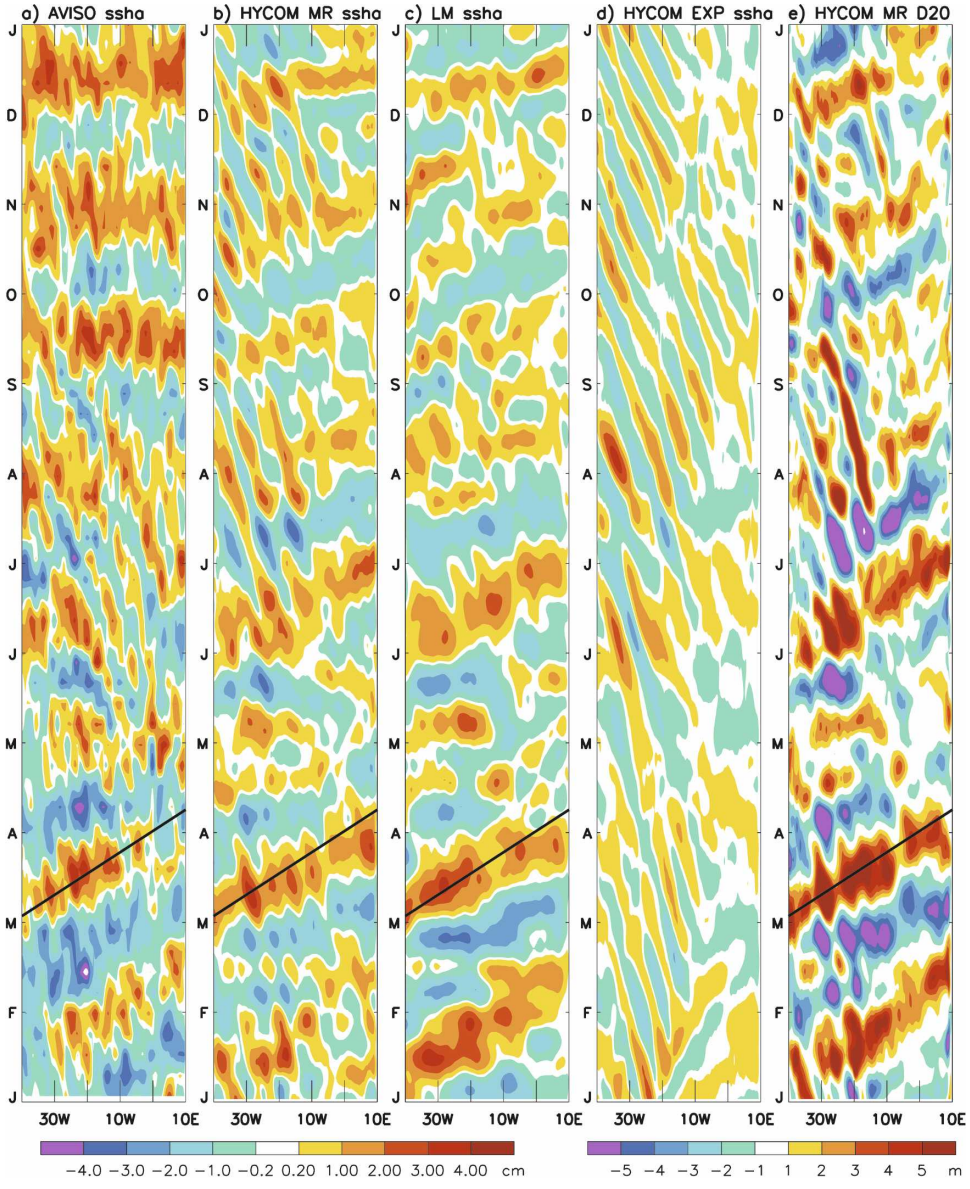

FIG. 4. Longitude–time plot of 14–80-day bandpassed SSHA along the equator (2°S–2°N average) during 2002 from (a) weekly AVISO observations, (b) daily HYCOM MR solution, (c) daily LM MR solution, (d) daily HYCOM EXP solution, which isolates the TIWs. (e) Same as in (b), but for HYCOM MR D20. AVISO and model data of 2001–03 are used for the filter. The dark solid lines in (a)–(c) and (e) show the SSHA and D20 phase lines. Units: cm for SSHA and m for D20.

tion (Fig. 4c), which demonstrates the deterministic role played by wind-driven equatorial-wave dynamics. During spring and early summer, intraseasonal SSHA and D20 exhibit an eastward phase propagation (the dark solid lines in Fig. 4) with a speed of approximately 174 cm s^{-1}, which is between that of the first and second baroclinic modes of the equatorial Kelvin waves (see Table 1). The westward-propagating, higher-frequency variability during summer results mainly from the TIWs (Fig. 4d), which are strong in northern summer. Variations of D20 basically mirror the SSHA (cf. Figs. 4e,b): when SSHA is high, thermocline deepens.

Figure 5 plots the variance spectra of SSHA averaged over 2°S–2°N from HYCOM MR, HYCOM EXP, and LM solutions for 2002–03. The 40–50-day variances extend across the equatorial Atlantic basin in both the HYCOM MR and LM solutions (Figs. 5a,c) but disappear in the HYCOM EXP run (Fig. 5b). This demonstrates that the 40–60-day, and especially the 40–50-day, SSHA is forced by intraseasonal winds rather than in-

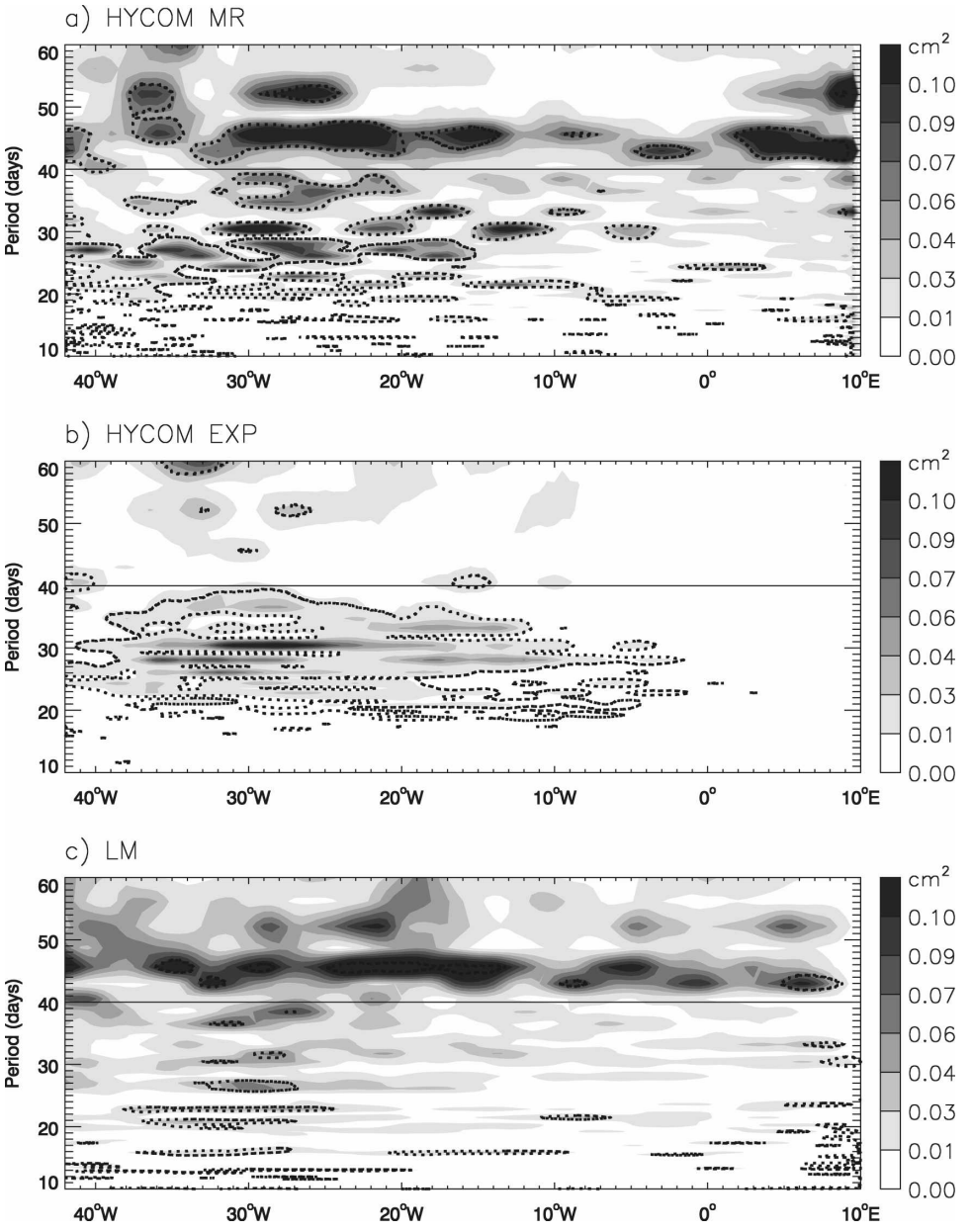

FIG. 5. (a) Variance spectra of SSHA along the equator (2°S–2°N average) based on daily HYCOM MR solution for the period of 2002–03; (b) same as in (a), but for HYCOM EXP; (c) same as in (a), but for LM MR solution. Dashed contours represent a 95% significance level.

duced by TIWs. Indeed, both the zonal and meridional wind stresses from QuikSCAT data exhibit strong 40–60-day periodicity, especially at 40–50 days in the equatorial Atlantic (Figs. 6a,b). The 40–50-day peaks are also present in the zonal wind stress of the NCEP–NCAR reanalysis data. However, the maximum power in the reanalysis product is in the western basin and is much weaker than the variance found in QuikSCAT wind in the central ocean (cf. Figs. 6a,c). Moreover, no spectral peaks appear in NCEP meridional wind stress at 40–50-day periods in the central basin (Fig. 6d). Consistent with the QuikSCAT winds (solid curves of Fig. 7), PIRATA data also show the largest spectral peaks at 40–50-day periods in zonal and meridional wind stresses at 35° and 23°W of the equator during 2002–03 (dashed curves).

To examine the spatial structure of the 40–50-day sea level oscillations, the 40–60-day bandpass-filtered SSHA for a case of spring 2002 is plotted in Fig. 8. This is a time when the 40–50-day variation dominates the

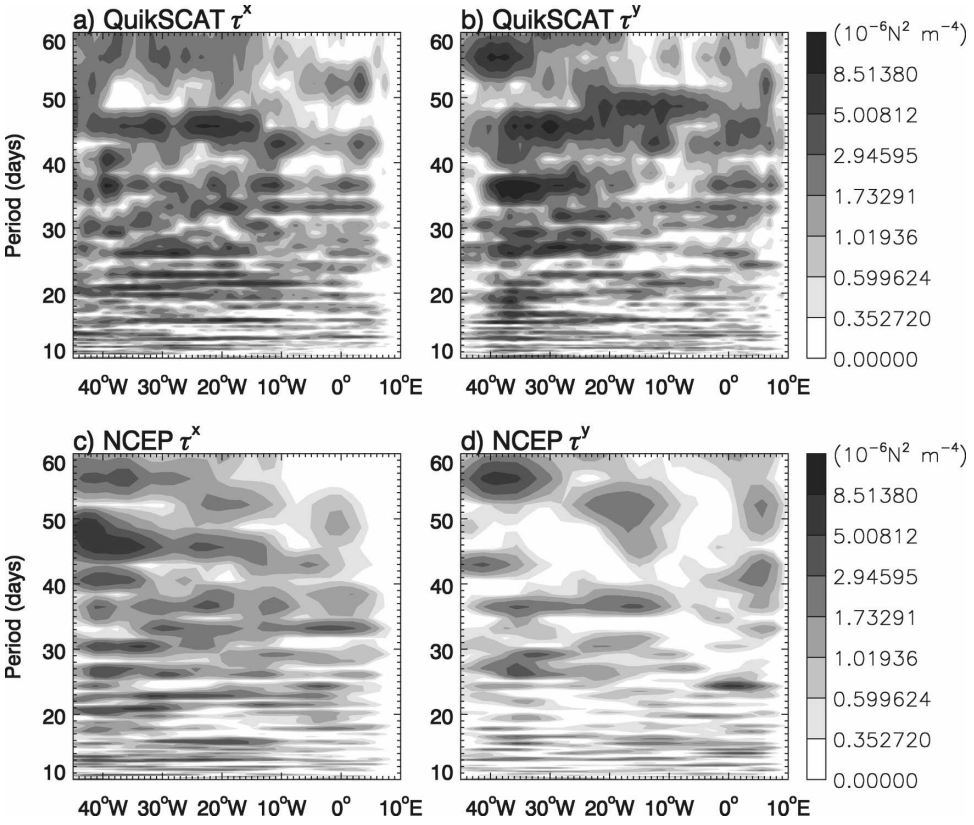

FIG. 6. Variance spectra of surface wind stress along the Atlantic equator (5°S–5°N average) based on daily winds of 2002–03. (a) QuikSCAT zonal wind stress, τ^x; (b) QuikSCAT meridional wind stress, τ^y; (c) NCEP τ^x; and (d) NCEP τ^y. As the QuikSCAT wind stress, NCEP wind stress is calculated from 10-m U and V winds using a drag coefficient of 0.0015.

intraseasonal SSHA (Fig. 4). Within the 3°S–3°N equatorial region, the observed SSHAs are dominated by wind-driven equatorial wave dynamics (Figs. 8a–i), and TIWs appear to play a minor role (Figs. 8j–l). The LM solution (Figs. 8g–i) exhibits an equatorial Kelvin-wave structure in the central and eastern basins, which is symmetric about the equator with decreasing amplitudes toward the poles. The wavelength is approximately 60° (Fig. 8i), which is between the first and second baroclinic modes of a Kelvin waves' length (80° and 46° at the 45-day period; Table 1). Note that the TIWs generally project their energy on Yanai and Rossby waves (Cox 1980), which have weak sea level amplitudes at the equator (Yuan 2005). In addition, the strong spectral peaks of TIWs generally occur at 10–40-day periods (see section 1) rather than at 40–60-day periods. All of these may contribute to the dominance of 40–60-day Kelvin waves, which obtain their maximum amplitudes on the equator. Away from the equator at 3°–5°N, SSHA is dominated by the TIWs even at the 40–60-day periods (Figs. 8j–l).

In the western equatorial basin, the LM SSHA shows the first meridional-mode Rossby-wave structure, with double maximum amplitudes off the equator and a relative minimum on the equator (Figs. 8g–i). The double maxima off the equator appear to be traceable in the AVISO data (Figs. 8a–c), although the structures are complicated by the presence of TIWs at 3°–5°N. The 40–60-day oscillations during fall have also been analyzed, producing results similar to those shown in Fig. 8.

Further inspection of the LM solutions suggest that the 40–60-day SSHA near the equator results mainly from the first two baroclinic modes' contribution with mode 2 possessing larger amplitudes than mode 1 (not shown). This is because mode 2 is more effectively excited by winds, with a wind coupling coefficient 2.6 times that of mode 1 (Table 1). Note that mode 3 is not effectively excited, even though its wind coupling coefficient is larger than that for mode 1. This is because amplitudes of Kelvin waves also depend on the spatial structure of forcing winds. Assume the ocean is forced by a stationary zonal wind stress τ^x. The amplitudes of a Kelvin or Rossby wave are proportional to the zonal integral of the product of the wind and the wave struc-

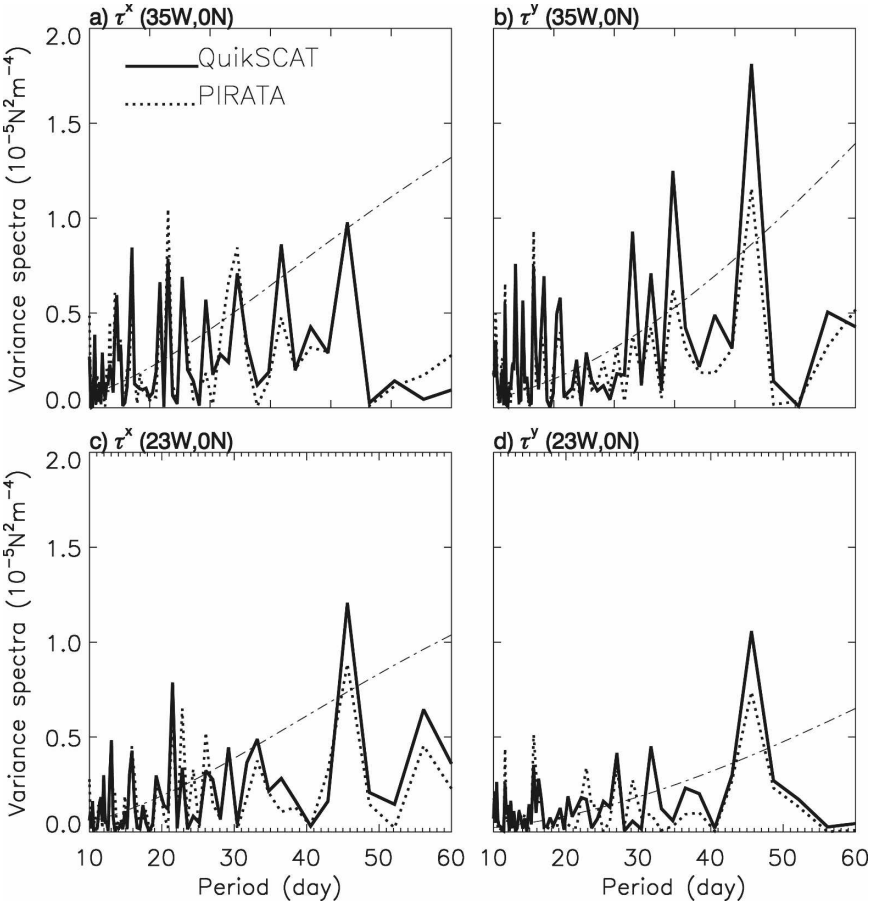

FIG. 7. (a) Variance spectra of τ^x at 0°, 35°W from daily QuikSCAT (solid) and PIRATA (dashed) data for the period of 2002–03. The dashed–dotted line is the 90% significance curve for the QuikSCAT data. The seasonal cycle is removed before performing the spectral analysis. (b) Same as in (a), but for τ^y; (c) Same as in (a), but for 23°W, 0°N; (d) Same as in (c), but for τ^y. The 1°S–1°N averaged values are shown for QuikSCAT winds.

ture, $\int \tau^x \, e^{-ikx} \, dx$, where k is the wavenumber of the Kelvin or Rossby wave. The amplitude thus depends on the parameter kL, where, in this case, L represents the zonal scale of the wind. If $kL \geq 1$, then e^{-ikx} oscillates within the region of the wind, producing an oscillating integral; when $kL \ll 1$, $e^{-ikx} \approx 1$ and the amplitude achieves its maximum possible value. The length of Kelvin wave associated with mode 1 is much longer than that of mode 3 (Table 1). Mode 1 is therefore more efficiently excited by the large-scale wind. Additionally, vertical mixing acts more strongly on the higher-order modes (McCreary 1980, 1985), and this also tends to reduce their amplitudes.

The strong 40–60-day westerly wind anomaly in the central-western basin causes equatorial convergence and raises the sea level (Figs. 9a–c). The high-SSHA signals propagate eastward as equatorial Kelvin waves (Figs. 9b,c). The importance of zonal wind stress in forcing Kelvin waves is quantified by Fig. 9d (cf. Fig. 9c). Interestingly, the complex spatial pattern of winds appears to enhance the wave response. For example, in early March, westerly winds along the equator excite mode 1 and mode 2 Kelvin waves that are associated with positive SSHA (Figs. 9a–c). In late March when the positive SSHA propagates to the eastern boundary, significant westerly winds appear over 10°W–10°E, which enhance the Kelvin-wave amplitudes in the region, especially for the first baroclinic mode. Figures 9a,b seem to show that zonal winds move eastward with oceanic Kelvin waves in the central-eastern basin during January–June. The enhanced Kelvin-wave response to the eastward-propagating wind was discussed by Hendon et al. (1998) for the Pacific and Han et al. (2001) for the Indian Ocean. It is not obvious, however, whether the winds in the western basin are actually propagating to the east or wheth-

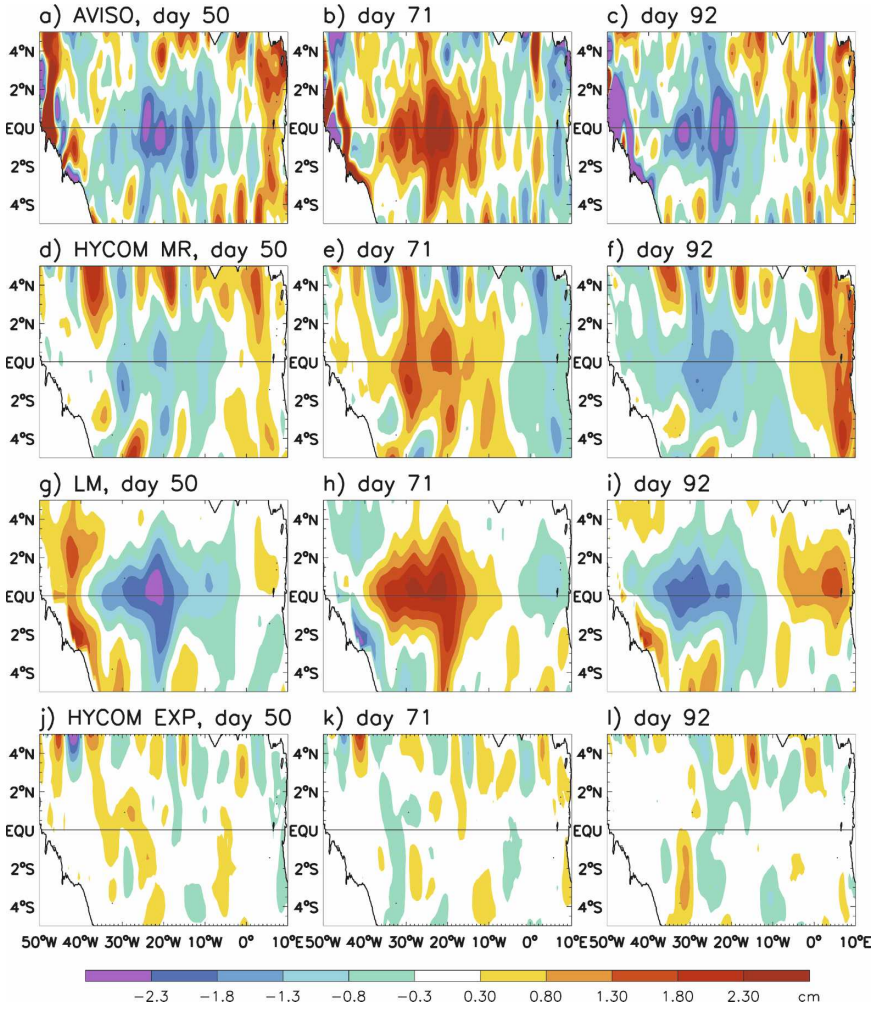

FIG. 8. (a) The 40–60-day bandpassed AVISO weekly SSHA in the equatorial Atlantic basin during spring, day 50 of 2002; (b), (c) Same as in (a), but for days 71 and 92; (d)–(f) same as in (a)–(c), but for SSHA from HYCOM MR solution; (g)–(i) same as in (a)–(c), but for SSHA from the wind-driven LM MR solution; (j)–(l) same as in (a)–(c), but for SSHA from HYCOM EXP, which excludes intraseasonal forcing and represents the effects of TIWs.

er the winds in the eastern and western basins originated from different atmospheric systems. During summer and especially fall, winds are weaker and the "propagation" feature disappears. The 40–60-day winds (Fig. 9a) also coincide with the observed intraseasonal SSHA, which is dominated by 40–60-day oscillations (Fig. 4a).

Given that the 40–60-day SSHA basically shows a symmetric Kelvin-wave structure (Fig. 8), Rossby waves, especially antisymmetric Rossby waves, are not excited effectively, even though strong spectral peaks exist in the meridional winds at this period band (Fig. 6b). This is because propagating Rossby waves are available only for the first baroclinic mode (Fig. 10), which is weakly coupled to the forcing winds (Table 1). The second baroclinic-mode Rossby waves only exist at periods longer than 45 days, and their wavelengths are too short (12° at the 50-day period; Table 1) to be excited efficiently by the large-scale winds.

The variance spectra of TRMM SST during 2002–03 also exhibit 40–60-day spectral peaks (Fig. 11a). This is consistent with the strong 40–60-day peaks of winds and D20. Time series of SST from TRMM and PIRATA data at 0°, 10°W, a location where 40–60-day SST has strong power, shows significant intraseasonal SST variations (Fig. 11b). The near 45-day oscillations of SST can be identified visually for the periods of January–April 2002 and June–August 2003, during which SST can vary as much as 2°–4°C. For example, at the beginning of April 2002, SST cools to 27°C, whereas by

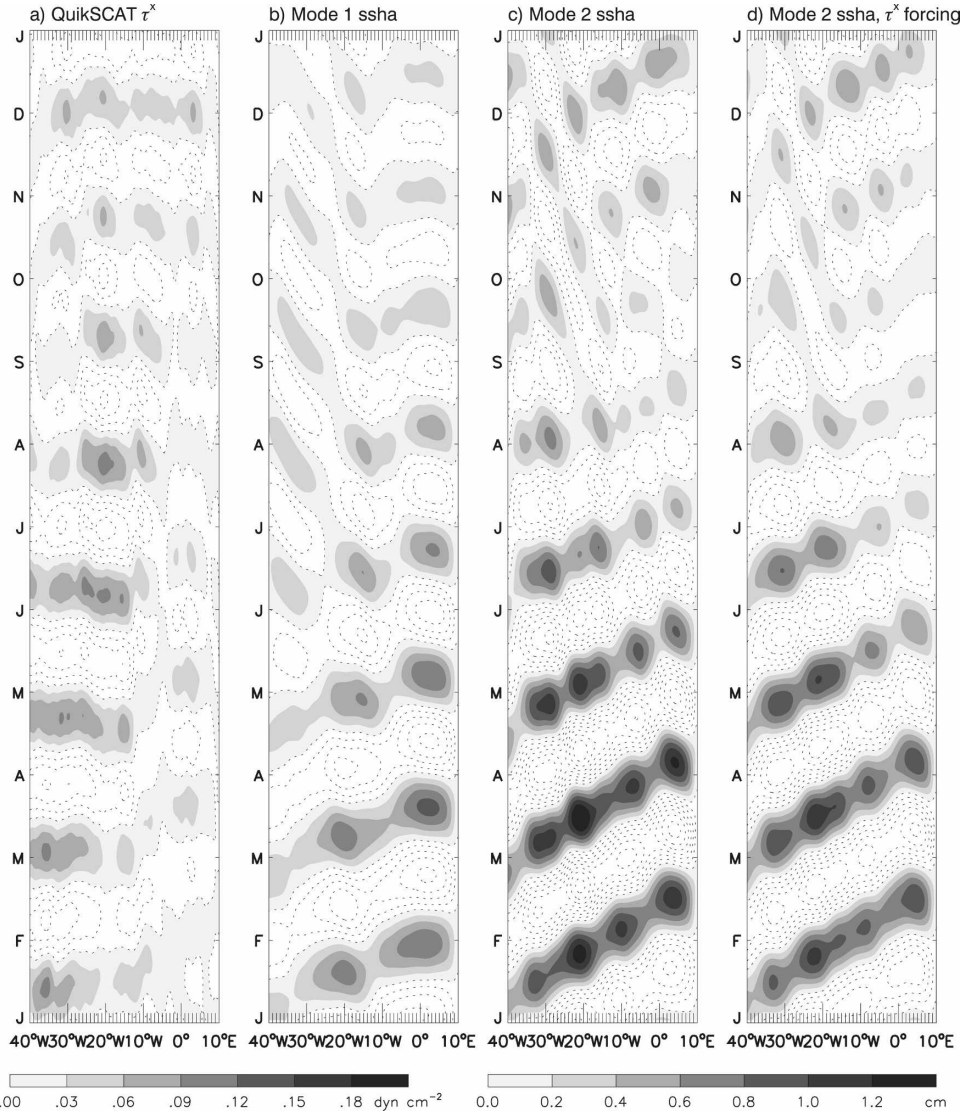

FIG. 9. (a) Longitude–time plot of 40–60-day bandpass-filtered QuikSCAT zonal wind stress along the equatorial Atlantic (5°S–5°N average) during 2002. Positive values are shaded and negative ones are contoured (dashed lines), with an interval of 0.03 dyn cm^{-2}. (b) Same as in (a), but for 2°S–2°N averaged 40–60-day SSHA from mode 1 of the LM MR solution. Positive values are shaded and negative ones are contoured, with an interval of 0.2 cm. (c) Same as in (b), but for mode 2. (d) Same as in (c), but for mode 2 of the LM EXP1, which is forced by zonal wind stress only.

the end of the month it warms to 31°C. Strong cooling at the end of July 2003 drops the SST to 22.5°C, while warming in late August increases the SST to 26°C. There is a strong correspondence between the SST measurements from PIRATA and estimates from the TRMM. Detailed examination on the relative importance of surface heat fluxes versus oceanic processes, including thermocline variability and mixed layer physics, in determining intraseasonal SST variability is beyond the scope of this paper, but it will be an essential part of our future research.

2) 1999–2006

Figure 12 shows the variance spectra of QuikSCAT wind stress and AVISO SSHA based on a 7-yr record of 2000–06. Both zonal and meridional winds have significant power for the entire 10–60-day periods, and there are relative spectral peaks at 40–50 days in the central basin (Figs. 12a,b). The SSHA spectra (Fig. 12c), however, have much stronger peaks at 40–50 days than found at the 10–40-day TIW periods in the central basin. Figure 13 shows correlation maps between the

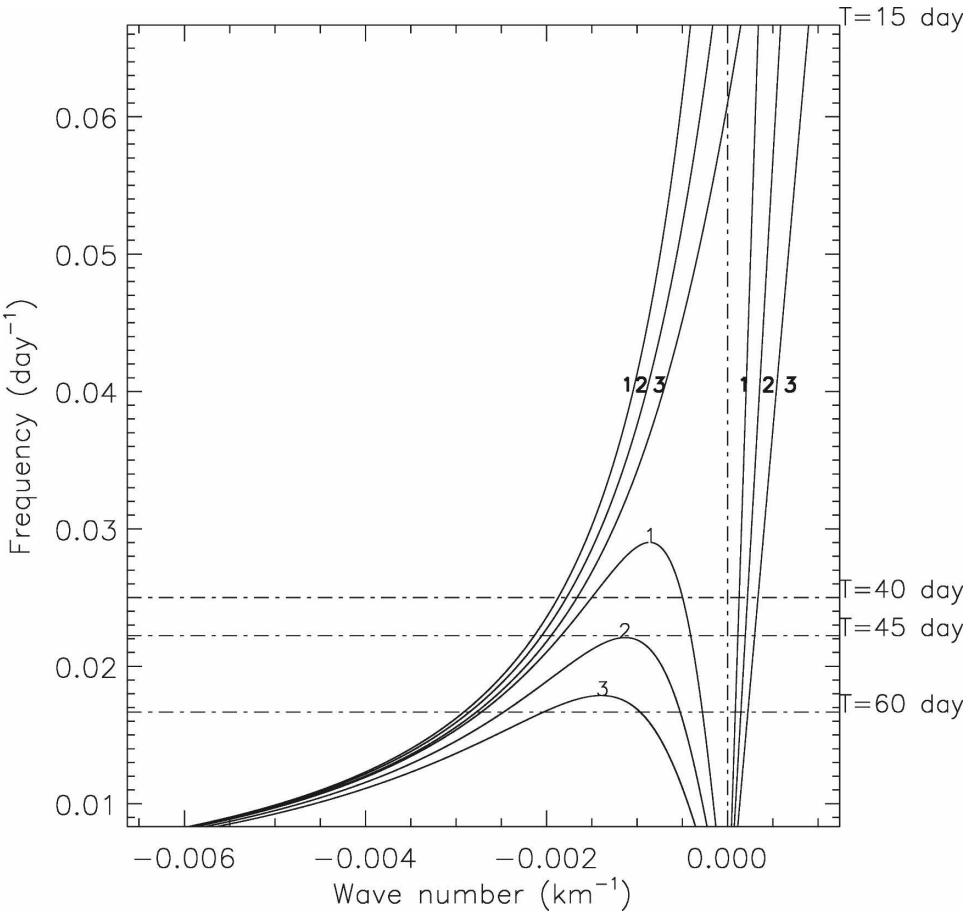

FIG. 10. Dispersion relations for equatorial Kelvin, Rossby, and Yanai waves for the first three baroclinic modes of the LM.

40–60-day zonal wind stress averaged over 2°S–2°N, 35°–10°W, a region where τ^x has a relative peak at 40–50 days (Fig. 12a), and SSHA at every grid point within 5°S–5°N. Daily QuikSCAT winds and weekly AVISO SSHA for the period of 1 August 1999–3 January 2007 are used to obtain the 40–60-day filtered fields. To remove the end point effects of the filter, data during February 2000–June 2006 are used to calculate the correlation in Figs. 13a,b. Simultaneous correlation between τ^x and SSHA shows a positive correlation west of 20°W and a negative correlation east of 20°W, with a strongest correlation of −0.62 (Fig. 13a). When SSHA lags the wind by 15 days, the correlation is positive in the central-eastern basin (Fig. 13b), with the maximum coefficient of 0.74 above the 95% significance level. The east–west out-of-phase correlation indicates the eastward propagation of oceanic Kelvin waves, as shown in Fig. 9. The τ^x–SSHA correlation is especially strong during 2002, with coefficients ranging from −0.96 to 0.91 above 90% significance for simultaneous and lag correlations (Figs. 13c,d). The strong correlation between winds and SSHA demonstrates the important role played by winds in causing the 40–60-day variability of sea level and thermocline in general, and especially for 2002.

c. *The 10–40-day variability*

In contrast to the 40–60-day SSHA that is dominated by the equatorially symmetric Kelvin waves within the 3°S–3°N equatorial belt, variations on 10–40-day time scales consist of both symmetric and antisymmetric components. In addition, TIWs have their maximum spectral peaks at the 10–40-day period band (e.g., Lyman et al. 2007).

Along the equator, the symmetric component (averaged over 2°S–2°N) of 10–40-day SSHA results largely from TIWs in the region west of 10°W (Fig. 5), with a maximum spectral peak occurring near the 30-day period. The wind-driven sea level variability, however, also appears to have considerable contributions (cf. Figs. 5a–c). East of 10°W, the 10–40-day SSHA power is relatively weak, and it is forced by the 10–40-day

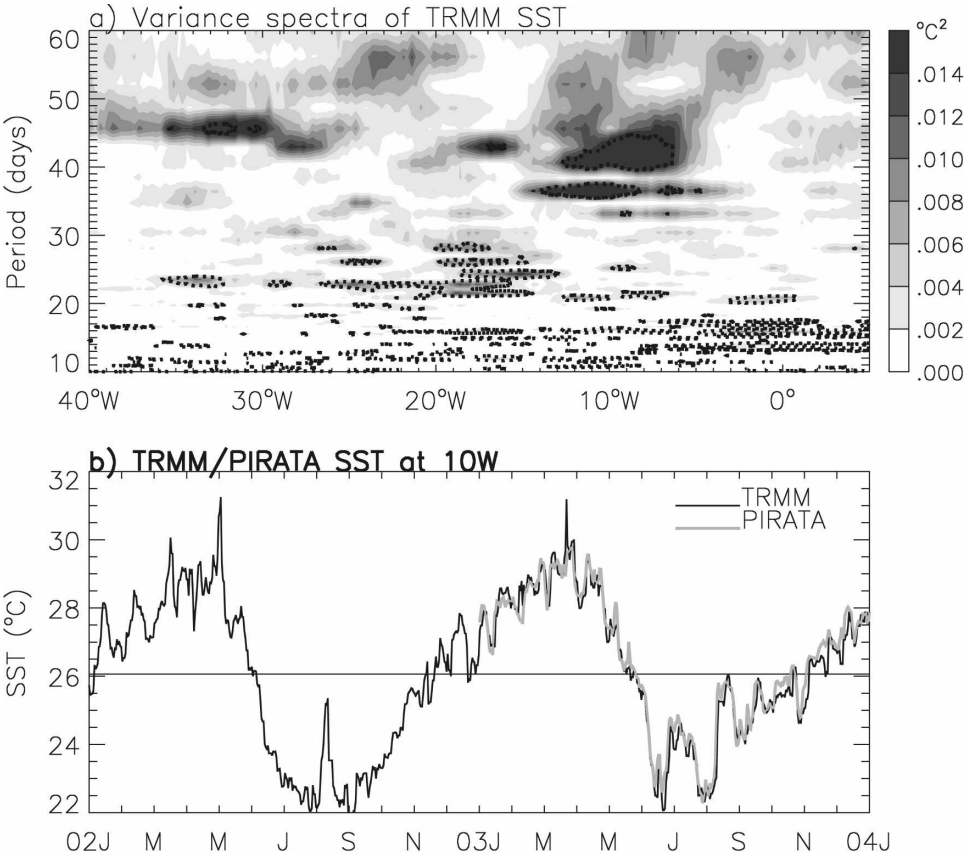

FIG. 11. (a) Variance spectra of SST averaged over 2°S–2°N of the Atlantic equator from 3-day-mean TRMM data for the period 2002–03. Dashed contours show a 90% significance level. (b) Time series of TRMM and PIRATA SST at 0°, 10°W during 2002–03. Note that continuous PIRATA SST is available only in 2003 at this location.

wind-possessing significant power at these periods (Fig. 6). The dominance of wind forcing in the eastern equatorial basin is also illustrated in Fig. 14. Interestingly, during January–May 2002 when the TIWs are relatively weak, wind forcing appears to dominate TIWs across the equatorial basin. Variations of D20 mirror those of SSHA (Figs. 14c,d). During June–December, both TIWs (Fig. 14b) and wind forcing (Fig. 14a) are important in the region west of 10°W (cf. Figs. 14a–c).

Off the equator at 2°–5°N, variability of sea level and thermocline in the eastern basin is still dominated by wind forcing (Fig. 15). West of 10°W, TIWs, which have westward phase propagation, play a dominant role during summer (cf. Figs. 15a–d). During spring and winter, both wind forcing and TIWs contribute. A similar situation holds near 2°–5°S (not shown). Interestingly, the LM solution shows large SSHA associated with quasi-biweekly Yanai waves during spring 2002, which are antisymmetric about the equator and have an eastward group velocity (March–May of Fig. 15a). This is consistent with the observational analysis of Bunge et al. (2006, 2007). By interacting with the TIWs, the Yanai waves complicate the sea level and thermocline variability (Figs. 15a–e). The Yanai waves appear to originate from the central–western basin and result mainly from the second baroclinic-mode response (not shown). They are forced primarily by the meridional wind stress τ^y (Fig. 15b), although wind-stress curl associated with τ^x also contributes to their formation (seen by the difference between Figs. 15a,b). Indeed, both τ^x and τ^y have relative spectral peaks at a quasi-biweekly period. These peaks, however, do not seem to be stronger than the winds at 20–40-day and 40–60-day periods (Fig. 6).

Why do the Yanai waves favor the biweekly period? At this relatively high frequency, the only available antisymmetric waves possible are Yanai waves, which have a small wavenumber and thus a long wavelength (Fig. 10; Table 1). Therefore, the Yanai waves are excited effectively by the basin-scale winds. Quasi-biweekly Yanai waves are also present in the equatorial Indian Ocean, where they dominate the meridional cur-

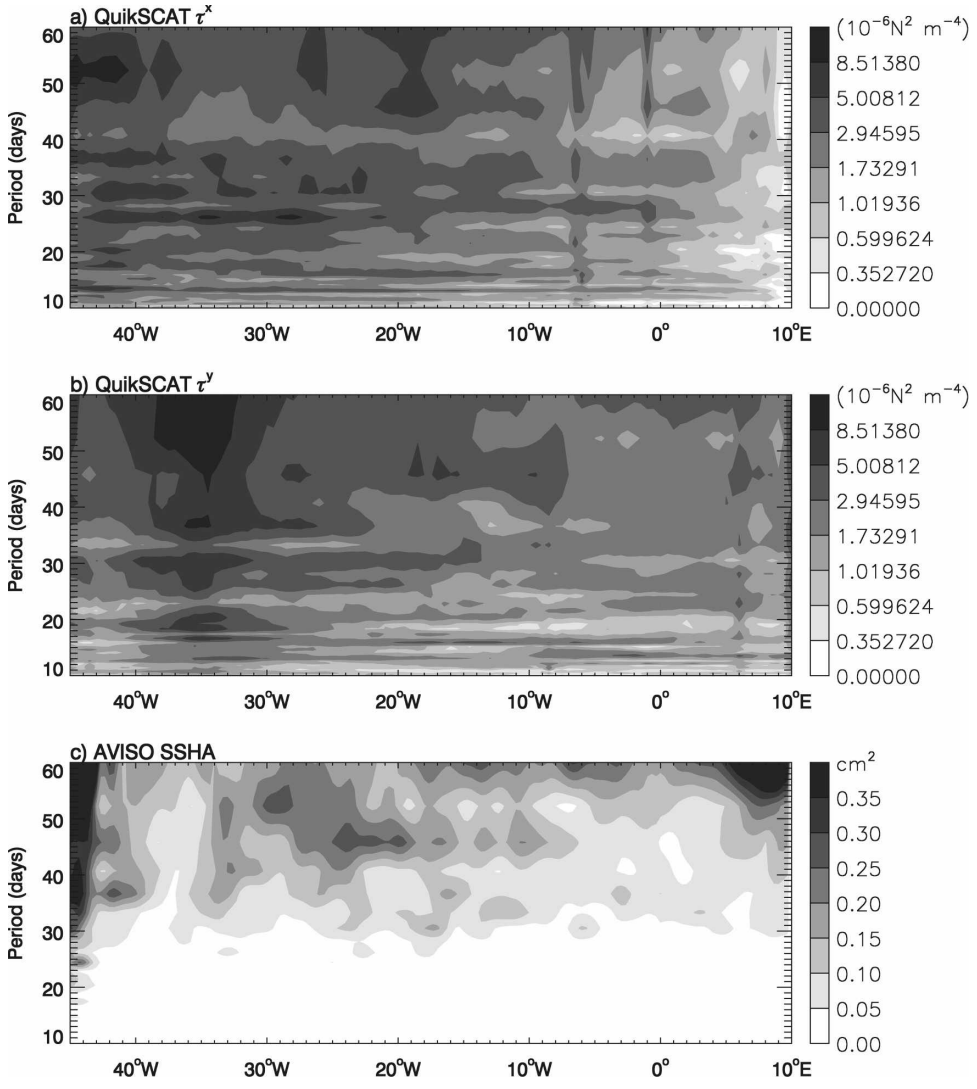

FIG. 12. (a) Variance spectra of QuikSCAT zonal wind stress τ^x, averaged over 5°S–5°N based on the 7-yr period 2000–06; (b) same as in (a), but for meridional wind stress τ^y. (c) Variance spectra of AVISO SSHA averaged over 2°S–2°N based on the period 2000–06.

rent variability (Masumoto et al. 2005; Miyama et al. 2006). At 40–60-day periods, Yanai waves are also available and higher-order baroclinic modes have longer wavelengths (not shown). These modes can also be excited by large-scale τ^y and $\partial\tau^x/\partial y$ in an inviscid ocean (Miyama et al. 2006). These modes, however, are strongly damped by vertical mixing and thus contribute weakly to the total solution (Miyama et al. 2006).

The spatial structures of SSHA associated with the Yanai waves are shown in Fig. 16 (right column). The SSHA attains its maximum amplitudes near 2–3°S and 2–3°N and oscillates at a period of approximately 2 weeks. The SSHA at the equator (Fig. 16g) results from equatorial Kelvin waves, as discussed above. The influence of Yanai waves on SSHA is seen clearly in the HYCOM MR (Figs. 16a–c). However, there are significant differences between the LM and HYCOM solutions due to the presence of TIWs and the nonlinearity of HYCOM. Note that TIWs have large amplitudes at 2°–5°N and 2°–5°S (Figs. 16d–f), and the associated SSHAs are symmetric about the equator in phase, consistent with the satellite observations (Chelton and Schlax 1996; Chelton et al. 2000; Lyman et al. 2005).

Correlation maps between 10–40-day QuikSCAT τ^x averaged over the central-western basin (45°–10°W, 2°S–2°N) and 10–40-day AVISO SSHA in the equatorial basin show a maximum coefficient of ~0.2 for the period 2000–06 and ~0.5 for 2002 (not shown). Correlations between τ^y and SSHA have similar amplitudes. Note, however, that to a large degree, the weaker wind-

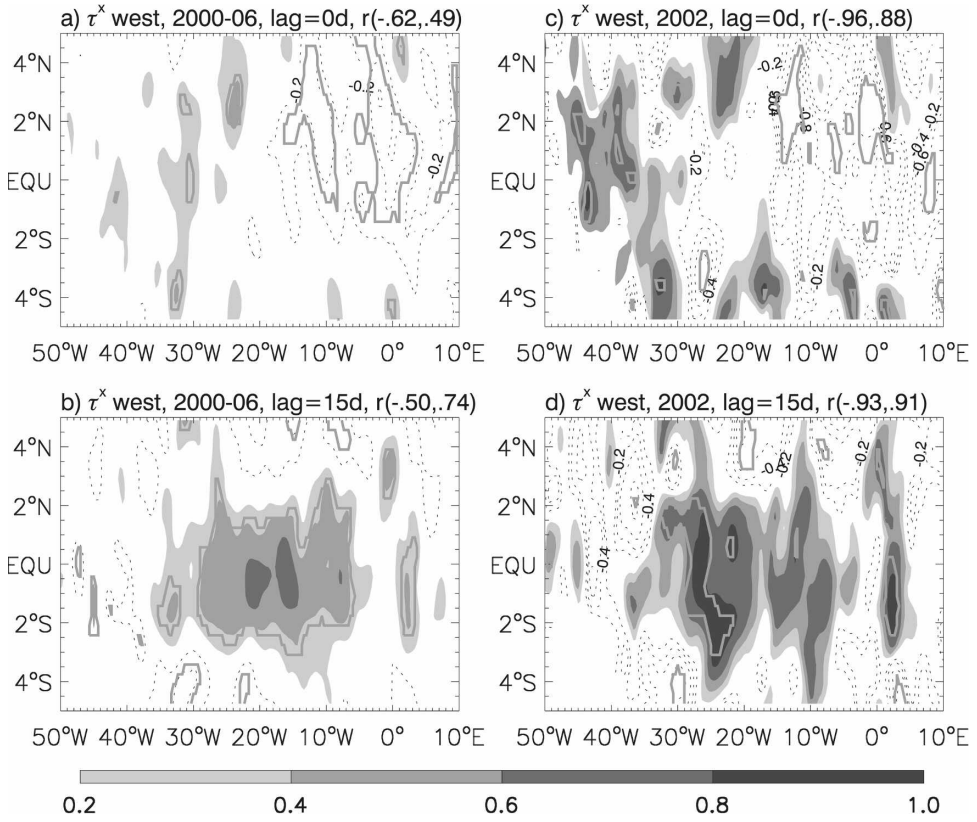

FIG. 13. (a) Simultaneous correlation map between time series of 40–60-day bandpass-filtered QuikSCAT zonal wind stress averaged over 2°S–2°N, 35°–10°W and 40–60-day AVISO SSHA in the equatorial Atlantic basin for the period 2000–06. Positive values are shaded and negative ones are contoured in dashed lines, with an interval of 0.2. The zero contour is suppressed. Correlation coefficients in regions within the thick solid gray lines exceed the 95% significance level. (b) Same as in (a), but with the SSHA lagging the wind by 15 days; (c) same as in (a), but for 2002. For this case, the thick solid gray lines represent a 90% significance level; (d) same as in (c), but with the SSHA lagging the wind by 15 days.

SSHA correlation on 10–40-day time scales may result from the interference between the forced waves and the strong TIWs. Even though intraseasonal winds have significant influence, the correlation can be weak due to the TIWs' interference.

d. Effects of TIW winds

Because TIWs can feedback to the atmosphere to induce wind changes (Xie et al. 1998; Liu et al. 2000; Chelton et al. 2001; Hashizume et al. 2001; Caltabiano et al. 2005), intraseasonal winds that force the ocean models include the TIW effect. A comparison of solutions from LM MR and LM EXP2 shows that neither the 40–60-day nor the 10–40-day SSHA is apparently altered by the TIW winds (not shown). The most visible contribution from the TIWs appears to occur during summer and fall in the central–western basin, where the TIWs are strong and their winds cause small-spatial-scale SSHA with westward phase propagation. Consequently, TIW winds do not seem to "overestimate" the wind-forced variability on intraseasonal time scales. Rather, they cause small-scale variability that appears to propagate westward with the TIWs.

4. Summary and discussion

In this paper, dominant spectral peaks within the intraseasonal window at 40–60 days are identified in sea level and thermocline depth along the Atlantic equator during the period 2002–03 (Figs. 1, 2). The peaks are especially strong and spatially coherent at 40–50 days during 2002 and are far stronger than the variance in the 10–40-day band associated with the TIWs within the 3°S–3°N equatorial region. The 10–80-day bandpass-filtered D20 varies from −15 to 13 m at 23°W during the 2002–03 period of interest (Fig. 2c). These ampli-

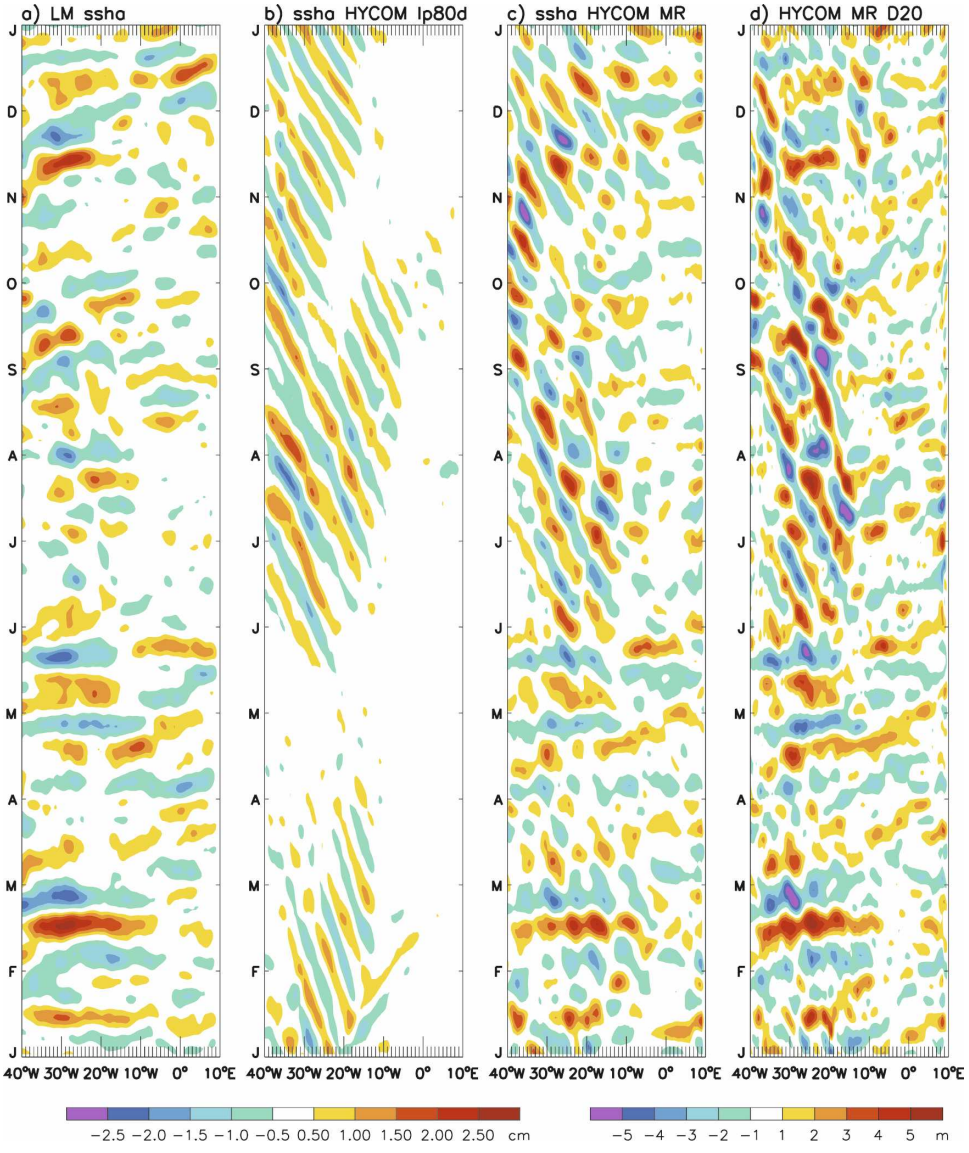

FIG. 14. (a) Longitude–time plot of 10–40-day bandpassed SSHA averaged over 2°S–2°N from the LM MR solution for 2002; (b) same as in (a), but for the HYCOM EXP run; (c) same as in (a), but for the HYCOM MR; (d) same as in (a), but for the HYCOM MR D20.

tudes are large compared to the PIRATA-mean D20 of 78 m. The results of diagnostic and modeling studies are presented to determine the relative role of wind-driven waves and TIWs in producing the observed intraseasonal variability in the equatorial Atlantic Ocean. The OGCM HYCOM is able to simulate the observed intraseasonal variability of SSHA, D20, and currents (Figs. 1–5) and to produce reasonable perturbation kinetic energy associated with the TIWs (section 3a).

The SSHA from both AVISO observations and model solutions shows an equatorial-Kelvin-wave structure and eastward phase propagation (Figs. 8, 4), demonstrating that the 40–60-day variability results from equatorial Kelvin waves driven by intraseasonal winds (Fig. 5). The QuikSCAT winds peak at 40–60-day, and especially at 40–50-day, periods in both zonal and meridional components across the equatorial basin (Fig. 6), and these peaks are also present in the PIRATA wind data (Fig. 7). The LM solution suggests further that the 40–60-day Kelvin waves are mainly forced by the zonal wind component and are dominated by the first two baroclinic modes, with the second mode playing a more important role (Fig. 9; Table 1). Sea level and D20 variations associated with the 40–60-day Kelvin waves have much larger amplitudes than the TIWs in the 3°S–3°N belt (Fig. 8) and dominate the

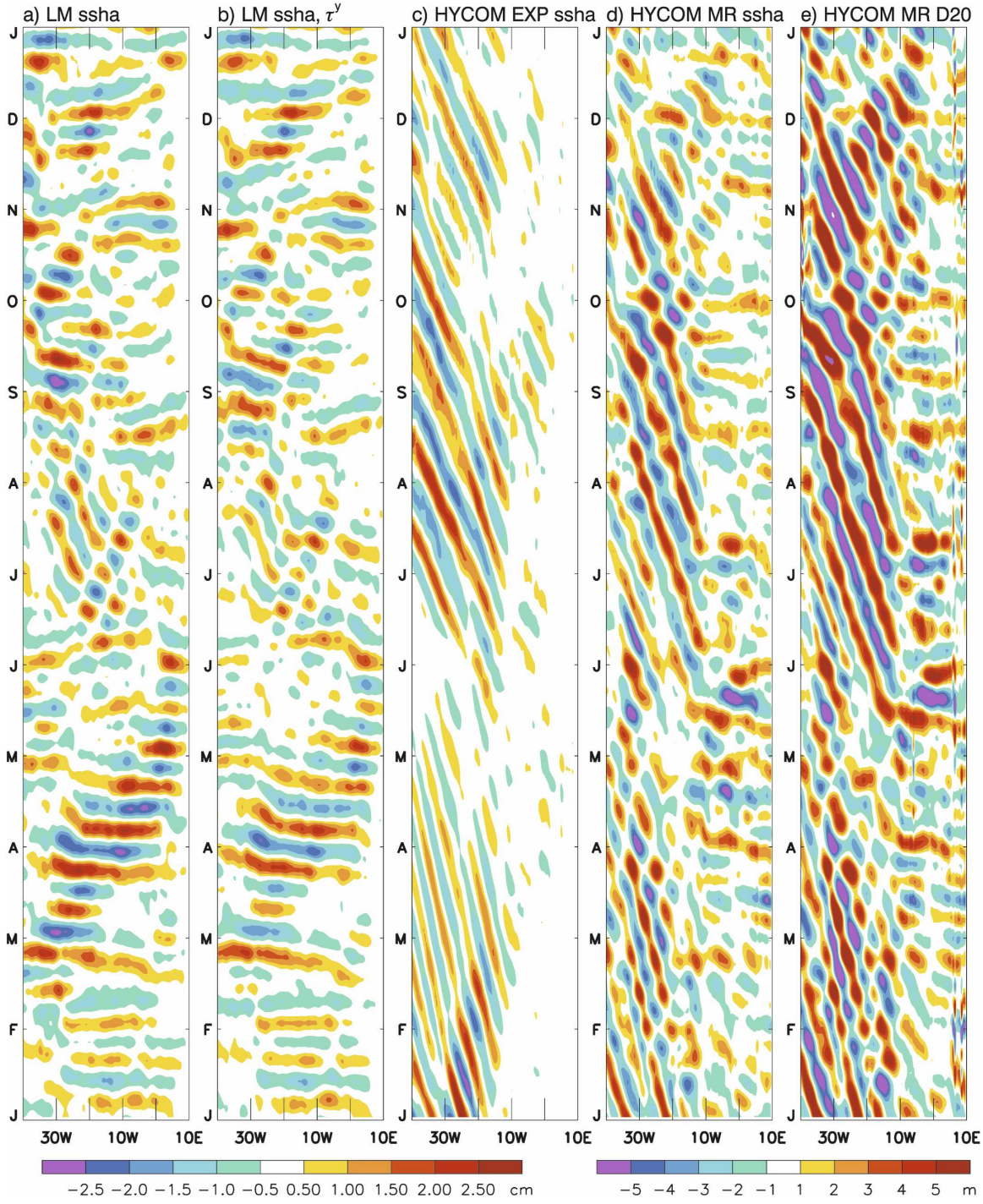

FIG. 15. (a) Longitude–time plot of 10–40-day bandpassed SSHA averaged over 2°–5°N from the LM MR solution for 2002; (b) same as in (a), but for LM (MR-EXP1), which isolates τ^y forcing; (c) same as in (a), but for the HYCOM EXP run; (d) same as in (a), but for the HYCOM MR; (e) same as in (d), but for the HYCOM MR D20.

10–40-day variability along the equator (Figs. 1, 2). Spectra of QuikSCAT zonal and meridional wind stress and AVISO SSHA for the 7-yr period 2000–06 also show relative peaks at 40–60 days (Fig. 12), and zonal wind stress in the central-western equatorial basin is significantly correlated with the SSHA in the equatorial region (Fig. 13), suggesting the importance of winds in driving the 40–60-day variability of SSHA and

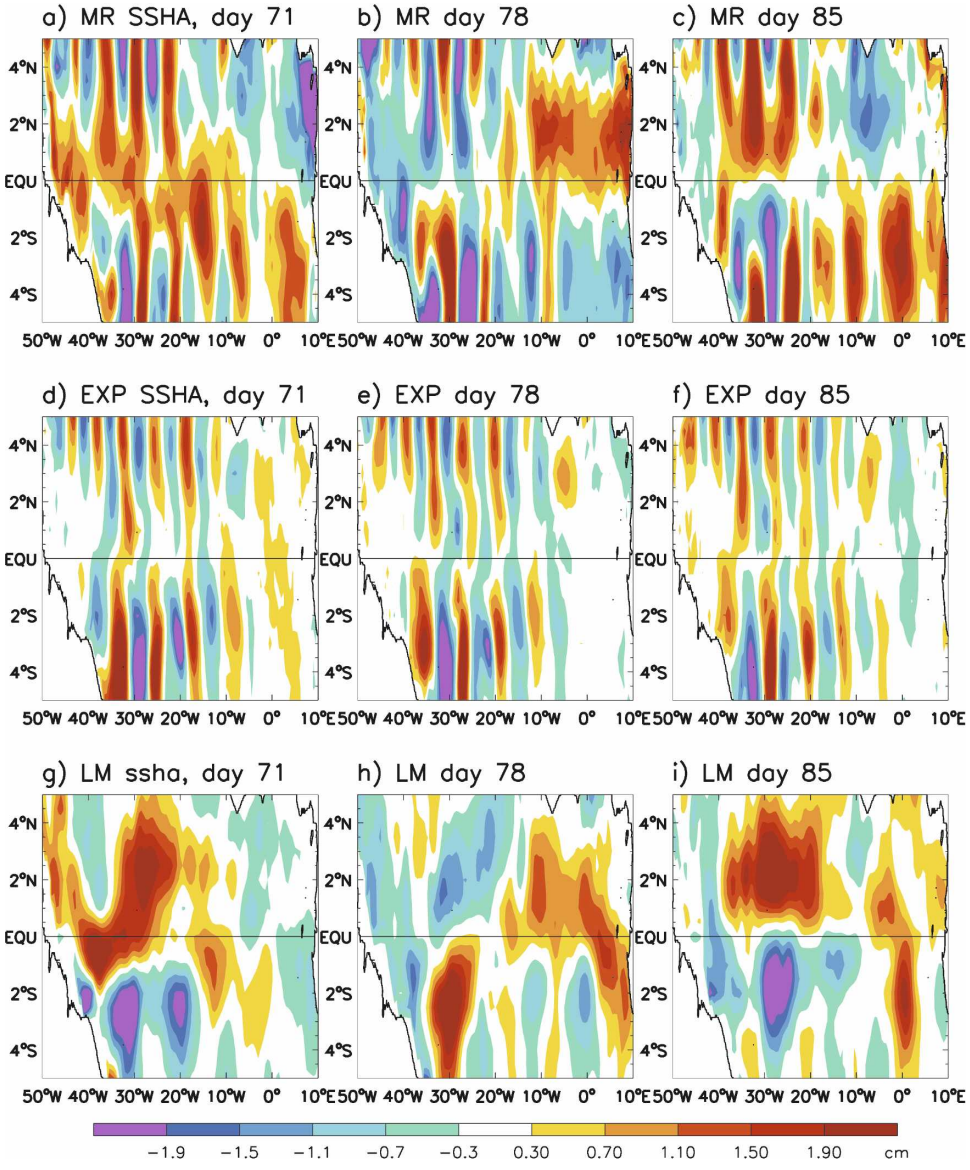

FIG. 16. (a) The 10–40-day bandpassed HYCOM MR SSHA in the equatorial Atlantic basin during spring, day 71 of 2002; (b), (c) same as in (a), but for days 78 and 85; (d)–(f) same as in (a)–(c), but for SSHA from HYCOM EXP; (g)–(i) same as in (a)–(c), but for SSHA from LM MR solution.

D20 in general. Away from the equator at 3–5°N and 3–5°S where TIWs are strong, the 40–60-day variability has comparable power with the 10–40-day variability, and the TIWs appear to dominate the wind-driven SSHA and thermocline variations at 40–60-day periods (Fig. 8).

Consistent with the sea level and thermocline depth variations, there are also 40–60-day spectral peaks in SST along the equator (Fig. 11) and corresponding SST changes by 2–4°C during March–April 2002 and June–August 2003. During boreal spring, mean SST is near 29°C and the ITCZ is very close to the equator (Xie and Carton 2004). At such a high SST, a 2°–4°C change of temperature may have a large impact on ITCZ convection.

On 10–40-day time scales, both SSHA and D20 are influenced by Kelvin waves, Yanai waves, and TIWs. West of 10°W, the spectral power of SSHA during 2002–03 is contributed significantly from TIWs along the equator (Fig. 5); SSHA and D20 are dominated by the TIWs at 2°–5°N and 2°–5°S during northern summer (Fig. 15). Wind-driven equatorial waves, however, also have significant contributions (Figs. 5, 15, 16). East of 10°W, sea level and thermocline variabilities are

caused almost entirely by wind-driven equatorial waves within 5°S–5°N of the equatorial ocean (Figs. 5, 14–16). Along the equator, during boreal spring 2002 when TIWs are weak, wind-forced equatorial Kelvin waves are the major cause for the SSHA and D20 variabilities, even in the central-western basin (west of 10°W; Fig. 14). In addition, Yanai waves are strongly excited by winds, especially the meridional winds at quasi-biweekly periods during spring 2002 (Figs. 15, 16), which have strong influence on the SSHA and D20 in the equatorial Atlantic basin.

A key result from this study is that intraseasonal variability in the equatorial Atlantic Ocean is not always dominated by the TIWs. Rather, the wind-driven equatorial waves play a crucial role. There are a number of immediate questions that come to mind: From where do the strong 40–50-day and 10–40-day surface-forcing winds emerge? Are they associated with the MJO that is generated in the tropical Indian and western Pacific Oceans (Foltz and McPhaden 2004), or do they originate from the Amazon convection as suggested by Wang and Fu (2007)? Are the quasi-biweekly winds that force the strong oceanic Yanai waves related to the quasi-biweekly winds of the West African monsoon (Grodsky and Carton 2001; Janicot and Sultan 2001)? It is the wind associated with the ISOs that produce large-amplitude variability in sea level and thermocline depth. Winds from the TIWs' feedback generate only weak SSHA with small spatial scale in the central-western basin during summer and fall (section 3d). How does the oceanic variability affect the ITCZ convection? How do the atmospheric ISOs affect the Atlantic El Niño? These are important questions that need to be addressed in future research.

Acknowledgments. We thank NOAA/CIRES Climate Diagnostics Center for making the NCEP–NCAR reanalysis data and CMAP precipitation available on the Internet, and Dr. Yuanchong Zhang for providing the ISCCP flux data. The PIRATA data were downloaded from the NOAA/PMEL Web site (http://www.pmel.noaa.gov/pirata; the altimeter data were downloaded from http://www.jason.oceanobs.com/html/donnees/produits/msla_uk.html). Appreciation also goes to Dr. Wendy Tang and Dr. Xiaosu Xie for preparing the QuikSCAT wind data. Weiqing Han was supported by NSF OCE-0452917 and NASA Ocean Vector Winds Program award 1283568, Peter J. Webster by NSF ATM-0531771, Jia-Lin Lin by NOAA-OGP/CVP and NASA MAP Programs, W. Timothy Liu by NASA Ocean Vector Winds and Physical Oceanography Programs, R. Fu by NASA Ocean Vector Winds Program and NOAA Climate Prediction Program for the Americas, D. Yuan by the National Basic Research of China ("973 program") project 2006CB403603, the "100-Expert Program" of the Chinese Academy of Sciences, and the NSF project 40676020, and Aixue Hu partly by the Office of Science (BER), U.S. Department of Energy, Cooperative Agreement No. DE-FC02-97ER62402. Aixue Hu is an employee at the National Center for Atmospheric Research. We also wish to thank the two anonymous reviewers, whose comments and suggestions improved our manuscript.

REFERENCES

Baturin, N. G., and P. P. Niiler, 1997: Effects of instability waves in the mixed layer of the equatorial Pacific. *J. Geophys. Res.,* **102,** 27 771–27 793.

Bleck, R., 2002: An oceanic general circulation model framed in hybrid isopycnic- Cartesian coordinates. *Ocean Modell.,* **4,** 55–88.

Brandt, P., F. A. Schott, C. Provost, A. Kartavtseff, V. Hormann, B. Bourlès, and J. Fischer, 2006: Circulation in the central equatorial Atlantic: Mean and intraseasonal to seasonal variability. *Geophys. Res. Lett.,* **33,** L07609, doi:10.1029/2005GL025498.

Bunge, L., C. Provost, J. M. Lilly, M. D'Orgeville, A. Kartavtseff, and J.-L. Melice, 2006: Variability of the horizontal velocity structure in the upper 1600 m of the water column on the equator at 10°W. *J. Phys. Oceanogr.,* **36,** 1287–1304.

——, ——, and A. Kartavtseff, 2007: Variability in horizontal current velocities in the central and eastern equatorial Atlantic in 2002. *J. Geophys. Res.,* **112,** C02014, doi:10.1029/2006JC003704.

Caltabiano, A. C. V., I. S. Robinson, and L. P. Pezzi, 2005: Multi-year satellite observations of instability waves in the Tropical Atlantic Ocean. *Ocean Sci. Discuss.,* **2,** 1–35.

Chelton, D. B., and M. G. Schlax, 1996: Global observations of oceanic Rossby waves. *Science,* **272,** 234–238.

——, F. J. Wentz, C. L. Gentemann, R. A. de Szoeke, and M. G. Schlax, 2000: Satellite microwave SST observations of transequatorial tropical instability waves. *Geophys. Res. Lett.,* **27,** 1239–1242.

——, and Coauthors, 2001: Observations of coupling between surface wind stress and sea surface temperature in the eastern tropical Pacific. *J. Climate,* **14,** 1479–1498.

Contreras, R. L., 2002: Long-term observations of tropical instability waves. *J. Phys. Oceanogr.,* **32,** 2715–2722.

Cox, M., 1980: Generation and propagation of 30-day waves in a numerical model of the Pacific. *J. Phys. Oceanogr.,* **10,** 1168–1186.

Ducet, N., P. Y. Le Traon, and G. Reverdin, 2000: Global high-resolution mapping of ocean circulation from TOPEX/Poseidon and ERS-1 and -2. *J. Geophys. Res.,* **105,** 19 477–19 498.

Duchon, C. E., 1979: Lanczos filtering in one and two dimensions. *J. Appl. Meteor.,* **18,** 1016–1022.

Dueing, W., and Coauthors, 1975: Meanders and long waves in the equatorial Atlantic. *Nature,* **257,** 280–284.

Foltz, G. R., and M. J. McPhaden, 2004: The 30-70 day oscillations in the tropical Atlantic. *Geophys. Res. Lett.,* **31,** L15025, doi:10.1029/2004GL020023.

Garzoli, S. L., 1987: Forced oscillations on the Equatorial Atlantic

Basin during the Seasonal Response of the Equatorial Atlantic Program (1983–1984). *J. Geophys. Res.,* **92,** 5089–5100.

Giarolla, E., P. Nobre, M. Malagutti, and L. P. Pezzi, 2005: The Atlantic Equatorial Undercurrent: PIRATA observations and simulations with GFDL Modular Ocean Model at CPTEC. *Geophys. Res. Lett.,* **32,** L10617, doi:10.1029/2004GL022206.

Grodsky, S. A., and J. A. Carton, 2001: Coupled land/atmosphere interactions in the West African Monsoon. *Geophys. Res. Lett.,* **28,** 1503–1506.

——, ——, C. Provost, J. Servain, J. A. Lorenzzetti, and M. J. McPhaden, 2005: Tropical instability waves at 0°N, 23°W in the Atlantic: A case study using Pilot Research Moored Array in the Tropical Atlantic (PIRATA) mooring data. *J. Geophys. Res.,* **110,** C08010, doi:10.1029/2005JC002941.

Halliwell, G. R., Jr., 1998: Simulation of North Atlantic decadal/multidecadal winter SST anomalies driven by basin-scale atmospheric circulation anomalies. *J. Phys. Oceanogr.,* **28,** 5–21.

——, 2004: Evaluation of vertical coordinate and vertical mixing algorithms in the Hybrid-Coordinate Ocean Model (HYCOM). *Ocean Modell.,* **7,** 285–322.

Halpern, D., R. A. Knox, and D. S. Luther, 1988: Observations of 20-day meridional current oscillations in the upper ocean along the Pacific equator. *J. Phys. Oceanogr.,* **18,** 1514–1534.

Han, W., 2005: Origins and dynamics of the 90-day and 30-60-day variations in the equatorial Indian Ocean. *J. Phys. Oceanogr.,* **35,** 708–728.

——, D. M. Lawrence, and P. J. Webster, 2001: Dynamical response of equatorial Indian Ocean to intraseasonal winds: Zonal flow. *Geophys. Res. Lett.,* **28,** 4215–4218.

——, P. J. Webster, R. Lukas, P. Hacker, and A. Hu, 2004: Impact of atmospheric intraseasonal variability in the Indian Ocean: Low-frequency rectification in equatorial surface current and transport. *J. Phys. Oceanogr.,* **34,** 1350–1372.

——, D. Yuan, W. T. Liu, and D. J. Halkides, 2007: Intraseasonal variability of Indian Ocean sea surface temperature during boreal winter: Madden–Julian Oscillation versus submonthly forcing and processes. *J. Geophys. Res.,* **112,** C04001, doi:10.1029/2006JC003791.

Hansen, D., and C. Paul, 1984: Genesis and the effect of long waves in the equatorial Pacific. *J. Geophys. Res.,* **89,** 10 431–10 440.

Hashizume, H., S.-P. Xie, W. Timothy Liu, and K. Takeuchi, 2001: Local and remote atmospheric response to tropical instability waves: A global view from space. *J. Geophys. Res.,* **106,** 10 173–10 185.

Hendon, H. H., B. Liebmann, and J. D. Glick, 1998: Oceanic Kelvin waves and the Madden–Julian oscillation. *J. Atmos. Sci.,* **55,** 88–101.

Houghton, R. W., and C. Colin, 1987: Wind-driven meridional eddy heat flux in the Gulf of Guinea. *J. Geophys. Res.,* **92,** 10 777–10 786.

Janicot, S., and B. Sultan, 2001: Intra-seasonal modulation of convection in the West African monsoon. *Geophys. Res. Lett.,* **28,** 523–526.

Jerlov, N. G., 1976: *Marine Optics.* Elsevier, 231 pp.

Jochum, M., P. Malanotte-Rizzoli, and A. Busalacchi, 2004: Tropical instability waves in the Atlantic Ocean. *Ocean Modell.,* **7,** 145–163.

Johnson, E. S., and J. A. Proehl, 2004: Tropical instability wave variability in the Pacific and its relation to large-scale currents. *J. Phys. Oceanogr.,* **34,** 2121–2147.

Kalnay, E., and Coauthors, 1996: The NCEP/NCAR 40-Year Reanalysis Project. *Bull. Amer. Meteor. Soc.,* **77,** 437–471.

Katz, E. J., 1987: Equatorial Kelvin waves in the Atlantic. *J. Geophys. Res.,* **92,** 1894–1898.

——, 1997: Waves along the equator in the Atlantic. *J. Phys. Oceanogr.,* **27,** 2536–2544.

Kennan, S. C., and P. J. Flament, 2000: Observations of a tropical instability vortex. *J. Phys. Oceanogr.,* **30,** 2121–2147.

Kessler, W. S., 2005: Intraseasonal variability in the oceans. *Intraseasonal Variability in the Atmosphere-Ocean System,* W. K. M. Lau and D. E. Waliser, Eds., Springer, 175–212.

Large, W. G., J. C. McWilliams, and S. C. Doney, 1994: Oceanic vertical mixing: A review and a model with a nonlocal boundary layer parameterization. *Rev. Geophys.,* **32,** 363–403.

——, G. Danabasoglu, S. C. Doney, and J. C. McWilliams, 1997: Sensitivity to surface forcing and boundary layer mixing in a global ocean model: Annual-mean climatology. *J. Phys. Oceanogr.,* **27,** 2418–2447.

Levitus, S., and T. P. Boyer, 1994: *Temperature*. Vol. 4, *World Ocean Atlas 1994,* NOAA Atlas NESDIS 4, 117 pp.

——, R. Burgett, and T. P. Boyer, 1994: *Salinity*. Vol 3, *World Ocean Atlas 1994,* NOAA Atlas NESDIS 3, 99 pp.

Legeckis, R., 1977: Long waves in the eastern equatorial Pacific Ocean: A view from a geostationary satellite. *Science,* **197,** 1179–1181.

——, and G. Reverdin, 1987: Long waves in the equatorial Atlantic Ocean during 1983. *J. Geophys. Res.,* **92,** 2835–2842.

Liu, W. T., X. Xie, P. S. Polito, S.-P. Xie, and H. Hashizume, 2000: Atmospheric manifestation of tropical instability wave observed by QuikSCAT and Tropical Rain Measuring Mission. *Geophys. Res. Lett.,* **27,** 2545–2548.

Luther, D. S., and E. S. Johnson, 1990: Eddy energetics in the upper equatrial Pacific during the Hawaii-to-Tahiti shuttle experiment. *J. Phys. Oceanogr.,* **20,** 913–944.

Lyman, J. M., D. B. Chelton, R. A. DeSzoeke, and R. M. Samelson, 2005: Tropical instability waves as a resonance between equatorial Rossby waves. *J. Phys. Oceanogr.,* **35,** 232–254.

——, G. C. Johnson, and W. S. Kessler, 2007: Distinct 17- and 33-day tropical instability waves in subsurface observations. *J. Phys. Oceanogr.,* **37,** 855–872.

Madden, R. A., and P. R. Julian, 1971: Detection of a 40–50-day oscillation in the zonal wind of the tropical Pacific. *J. Atmos. Sci.,* **28,** 702–708.

——, and ——, 1972: Description of global-scale circulation cells in the tropics with a 40–50-day period. *J. Atmos. Sci.,* **29,** 1109–1123.

Malardé, J.-P., C. Perigaud, P. de Mey, and J.-F. Minster, 1987: Observations of long equatorial waves in the Pacific Ocean by Seasat altimetry. *J. Phys. Oceanogr.,* **17,** 2273–2279.

Masina, S., S. G. H. Philander, and A. B. G. Bush, 1999: An analysis of tropical instability waves in a numerical model of the Pacific Ocean. 2. Generation and energetics of the waves. *J. Geophys. Res.,* **104,** 29 637–29 662.

Masumoto, Y., H. Hase, Y. Kuroda, H. Matsuura, and K. Takeuchi, 2005: Intraseasonal variability in the upper layer currents observed in the eastern equatorial Indian Ocean. *Geophys. Res. Lett.,* **32,** L02607, doi:10.1029/2004GL021896.

McCreary, J. P., 1980: Modeling wind-driven ocean circulation. Hawaii Institute of Geophysics Tech. Rep. HIG-80-3, 64 pp.

——, 1985: Modeling equatorial ocean circulation. *Annu. Rev. Fluid Mech.,* **17,** 359–409.

——, and Z. Yu, 1992: Equatorial dynamics in a 2.5-layer model. *Prog. Oceanogr.,* **29,** 61–132.

——, W. Han, D. Shankar, and S. R. Shetye, 1996: Dynamics of the East India Coastal Current 2. Numerical solutions. *J. Geophys. Res.,* **101,** 13 993–14 010.

McPhaden, M. J., 1996: Monthly period oscillations in the Pacific North Equatorial Countercurrent. *J. Geophys. Res.,* **101,** 6337–6359.

Miller, L., D. R. Watts, and M. Wimbush, 1985: Oscillations of dynamic topography in the eastern equatorial Pacific. *J. Phys. Oceanogr.,* **15,** 1759–1770.

Miyama, T., J. P. McCreary, D. Sengupta, and R. Senan, 2006: Dynamics of biweekly oscillations in the equatorial Indian Ocean. *J. Phys. Oceanogr.,* **36,** 827–846.

Musman, S., 1989: Sea height wave form in equatorial waves and its interpretation. *J. Geophys. Res.,* **94,** 3303–3309.

——, 1992: Geosat altimeter observations of long waves in the equatorial Atlantic. *J. Geophys. Res.,* **97,** 3573–3579.

Perigaud, C., 1990: Sea level oscillations observed with Geosat along the two shear fronts of the Pacific North Equatorial Countercurrent. *J. Geophys. Res.,* **95,** 7239–7248.

Philander, S., 1976: Instabilities of zonal equatorial currents . *J. Geophys. Res.,* **81,** 3725–3735.

——, 1978: Instabilities of zonal equatorial currents, 2. *J. Geophys. Res.,* **83,** 3679–3682.

Proehl, J. A., 1996: Linear stability of equatorial zonal flows. *J. Phys. Oceanogr.,* **26,** 601–621.

Qiao, L., and R. H. Weisberg, 1995: Tropical instability wave kinematics: Observations from the Tropical Instability Wave Experiment. *J. Geophys. Res.,* **100,** 8677–8693.

Richardson, P., and S. Philander, 1987: The seasonal variations of surface currents in the tropical Atlantic Ocean: A comparison of ship drift data with results from a general circulation model. *J. Geophys. Res.,* **92,** 715–724.

Servain, J., A. J. Busalacchi, M. J. McPhaden, A. D. Moura, G. Reverdin, M. Vianna, and S. E. Zebiak, 1998: A Pilot Research Moored Array in the Tropical Atlantic (PIRATA). *Bull. Amer. Meteor. Soc.,* **79,** 2019–2031.

Steger, J., and J. Carton, 1991: Long waves and eddies in the tropical Atlantic Ocean: 1984–1990. *J. Geophys. Res.,* **96,** 15 161–15 171.

Tang, W., and W. T. Liu, 1996: Objective interpolation of scatterometer winds. Jet Propulsion Laboratory Tech. Rep. 96-19, California Institute of Technology, 16 pp.

Thorncroft, C. D., and Coauthors, 2003: The JET2000 project: Aircraft observations of the African easterly jet and African easterly waves. *Bull. Amer. Meteor. Soc.,* **84,** 337–351.

Vangriesheim, A., A. M. Treguier, and G. Andre, 2005: Biweekly current oscillations on the continental slope of the Gulf of Guinea. *Deep-Sea Res. I,* **52,** 2168–2183.

Wang, H., and R. Fu, 2007: The influence of Amazon rainfall on the Atlantic ITCZ through convectively coupled Kelvin waves. *J. Climate,* **20,** 1188–1201.

Weisberg, R. H., 1984: Instability waves observed on the equator in the Atlantic Ocean during 1983. *Geophys. Res. Lett.,* **11,** 753–756.

——, and A. M. Horigan, 1981: Low-frequency variability in the equatorial Atlantic. *J. Phys. Oceanogr.,* **11,** 913–920.

——, and C. Colin, 1986: Equatorial Atlantic Ocean temperature and current variations during 1983 and 1984. *Nature,* **322,** 240–243.

——, and T. J. Weingartner, 1988: Instability waves in the equatorial Atlantic Ocean. *J. Phys. Oceanogr.,* **18,** 1641–1657.

——, A. M. Horigan, and C. Colin, 1979: Equatorially trapped Rossby-gravity wave propagation in the Gulf of Guinea. *J. Mar. Res.,* **37,** 67–86.

Wentz, F. J., C. Gentemann, D. Smith, and D. Chelton, 2000: Satellite measurements of sea surface temperature through clouds. *Science,* **288,** 847–850.

Xie, P., and P. A. Arkin, 1996: Analyses of global monthly precipitation using gauge observations, satellite estimates, and numerical model predictions. *J. Climate,* **9,** 840–858.

Xie, S. P., and J. A. Carton, 2004: Tropical Atlantic variability: Patterns, mechanisms, and impacts. *Earth Climate: The Ocean–Atmosphere Interaction, Geophys. Monogr.,* Vol. 147, Amer. Geophys. Union, 121–142.

——, M. Ishiwatari, H. Hashizume, and K. Takeuchi, 1998: Coupled ocean-atmospheric waves on the equatorial front. *Geophys. Res. Lett.,* **25,** 3863–3866.

Yu, Z., J. P. McCreary, and J. Proehl, 1995: Meridional asymmetry and energetics of tropical instability waves. *J. Phys. Oceanogr.,* **25,** 2997–3007.

Yuan, D., 2005: Role of the Kelvin and Rossby waves in the seasonal cycle of the equatorial Pacific Ocean circulation. *J. Geophys. Res.,* **110,** C04004, doi:10.1029/2004JC002344.

——, and W. Han, 2006: Roles of equatorial waves and western boundary reflection in the seasonal circulation of the equatorial Indian Ocean. *J. Phys. Oceanogr.,* **36,** 930–944.

Zhang, Y., W. B. Rossow, A. A. Lacis, V. Oinas, and M. I. Mishchenko, 2004: Calculation of radiative fluxes from the surface to top of atmosphere based on ISCCP and other global datasets: Refinements of the radiative transfer model and the input data. *J. Geophys. Res.,* **109,** D19105, doi:10.1029/2003JD004457.